

Differential Nanoscale Topography and Functional Role of GluN2-NMDA Receptor Subtypes at Glutamatergic Synapses

Blanka Kellermayer,^{1,2,3,9,*} Joana S. Ferreira,^{1,2,9} Julien Dupuis,^{1,2,9} Florian Levet,^{1,2,4,10} Dolores Grillo-Bosch,^{1,2,10} Lucie Bard,^{1,2,7,10} Jeanne Linares-Loyez,^{5,6} Delphine Bouchet,^{1,2} Daniel Choquet,^{1,2,4} Dmitri A. Rusakov,⁷ Pierre Bon,^{5,6} Jean-Baptiste Sibarita,^{1,2} Laurent Cognet,^{5,6} Matthieu Sainlos,^{1,2} Ana Luisa Carvalho,^{3,8} and Laurent Groc^{1,2,11,*}

¹Université de Bordeaux, Interdisciplinary Institute for Neuroscience, UMR 5297, 33000 Bordeaux, France

²CNRS, IINS UMR 5297, Bordeaux, France

³CNC—Center for Neuroscience and Cell Biology, University of Coimbra, 3004-504 Coimbra, Portugal

⁴CNRS, Bordeaux Imaging Center UMS 3420, 33000 Bordeaux, France

⁵Institut d'Optique & CNRS, LP2N UMR 5298, 33400 Talence, France

⁶Université de Bordeaux, Laboratoire Photonique Numérique et Nanosciences, UMR 5298, 33400 Talence, France

⁷UCL Institute of Neurology, University College London, London, UK

⁸Department of Life Sciences, Faculty of Sciences and Technology, University of Coimbra, 3004-517 Coimbra, Portugal

⁹These authors contributed equally

¹⁰These authors contributed equally

¹¹Lead Contact

*Correspondence: blanka.kellermayer@u-bordeaux.fr (B.K.), laurent.groc@u-bordeaux.fr (L.G.)

<https://doi.org/10.1016/j.neuron.2018.09.012>

SUMMARY

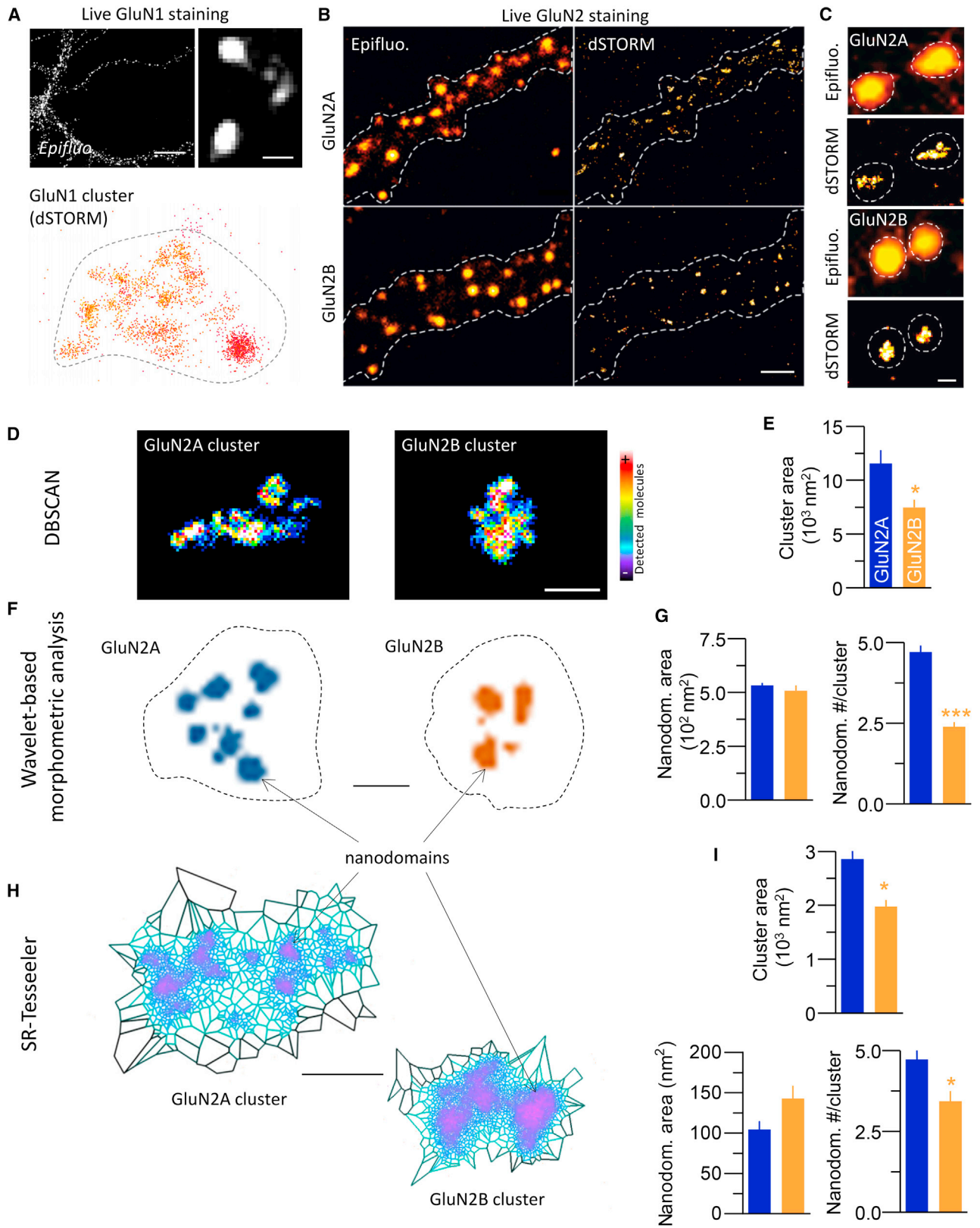
NMDA receptors (NMDARs) play key roles in the use-dependent adaptation of glutamatergic synapses underpinning memory formation. In the forebrain, these plastic processes involve the varied contributions of GluN2A- and GluN2B-containing NMDARs that have different signaling properties. Although the molecular machinery of synaptic NMDAR trafficking has been under scrutiny, the postsynaptic spatial organization of these two receptor subtypes has remained elusive. Here, we used super-resolution imaging of NMDARs in rat hippocampal synapses to unveil the nanoscale topography of native GluN2A- and GluN2B-NMDARs. Both subtypes were found to be organized in separate nanodomains that vary over the course of development. Furthermore, GluN2A- and GluN2B-NMDAR nanoscale organizations relied on distinct regulatory mechanisms. Strikingly, the selective rearrangement of GluN2A- and GluN2B-NMDARs, with no overall change in NMDAR current amplitude, allowed bi-directional tuning of synaptic LTP. Thus, GluN2A- and GluN2B-NMDAR nanoscale organizations are differentially regulated and seem to involve distinct signaling complexes during synaptic adaptation.

INTRODUCTION

Glutamatergic synapses mediate most of the excitatory neurotransmissions in the brain and adapt their strength to salient

stimuli, often by involving the glutamate NMDA receptor (NMDAR) (Yashiro and Philpot, 2008). The role of NMDARs in the central nervous system has thus been extensively studied using genetic and pharmacological manipulations. NMDARs are heterotetramers comprising various combinations of GluN1, GluN2A-D, and GluN3A-B subunits that confer specific biophysical and pharmacological properties to the receptor (Paoletti et al., 2013), with GluN2A- and GluN2B-containing receptors being the predominant forms of NMDARs found in the forebrain. The relative content of GluN2A and GluN2B subunits directly influences long-term plasticity at forebrain synapses and varies during brain development and sensory experience, and between brain hemispheres (Ito et al., 2000; Kawakami et al., 2003; Lau and Zukin, 2007; Smith et al., 2009; Yashiro and Philpot, 2008). Although it is well established that both receptor subtypes play important roles in synaptic adaptations, the specific involvement of GluN2A- and GluN2B-NMDARs in long-term potentiation (LTP) is still a matter of debate (Shipton and Paulsen, 2013; Yashiro and Philpot, 2008), which is likely attributable to the lack of appropriate pharmacological or genetic tools to finely dissect the GluN2A/2B contributions to NMDAR-mediated signaling (Bartlett et al., 2007; Berberich et al., 2005; Fox et al., 2006; Izumi et al., 2006; Li et al., 2007; Liu et al., 2004; Romberg et al., 2009). In addition, rapid modifications of the GluN2A/2B ratio occur shortly after the induction of synaptic potentiation in young hippocampal neurons through fast redistribution of surface receptors (Bellone and Nicoll, 2007; Dupuis et al., 2014; Matta et al., 2011), thus adding an additional layer of complexity in defining the exact role of GluN2 subunits in synaptic plasticity.

The synaptic content of GluN2A- and GluN2B-NMDARs is regulated by exocytosis, endocytosis, and lateral diffusion processes (Bard and Groc, 2011; Lussier et al., 2015; Paoletti et al., 2013). Once at the synapse, the anchoring of GluN2A- and



(legend on next page)

GluN2B-NMDARs greatly depends on their cytoplasmic C-terminal tails that contain motifs for protein-protein interaction and phosphorylation (Lussier et al., 2015). Although these mechanisms undoubtedly control the NMDAR synaptic content, distinct scaffold proteins and protein kinases have been identified to act on either GluN2A- or GluN2B-NMDARs, opening the possibility for different regulatory pathways and complexes (Lussier et al., 2015). Electron microscopy studies have suggested that the distributions of GluN2A- and GluN2B-NMDARs in the postsynaptic compartment and their regulatory mechanisms are distinct (Park et al., 2008; Shinohara et al., 2008). However, the nanoscale organization of GluN2A- and GluN2B-NMDAR pools within the postsynaptic compartment and the underlying molecular regulatory machinery remain an enigma.

Recent advances in super-resolution fluorescence microscopy enable imaging individual membrane receptors with subdiffraction resolution (Liu et al., 2015; Sahl et al., 2017; Zhuang, 2009). Among super-resolution approaches (Godin et al., 2014), the single-molecule localization microscopy (SMLM) techniques, such as direct stochastic optical reconstruction microscopy (dSTORM) (Heilemann et al., 2008), are effective tools to establish the molecular architecture of subcellular structures such as synapses. By determining the position of single fluorescent molecules with nanometer-scale precision, SMLM allows the nanoscale reconstruction of molecular assemblies. These approaches have been successfully applied to unveil the organization of neurotransmitter receptors in neuronal networks. In particular, the AMPA and GABA_A receptors are organized in nanoscale domains in postsynaptic densities of excitatory and inhibitory synapses, respectively (MacGillavry et al., 2013; Nair et al., 2013; Pennacchietti et al., 2017; Specht et al., 2013). Functionally, it has been proposed that these nanodomains of neurotransmitter receptors and scaffold proteins are dynamically regulated and control synaptic transmission through the alignment of pre- and postsynaptic molecular complexes (Tang et al., 2016). Presynaptically localized receptors and channels have also been investigated using super-resolution imaging, revealing the functional relevance of such nanoscale

organizations (Dudok et al., 2015; Ehmann et al., 2014; Zhan et al., 2014). Here, we used SMLM imaging, single-nanoparticle tracking, and electrophysiological recordings to investigate the dynamic nanoscale organization of native GluN2A- and GluN2B-NMDAR and its role in the adaptation of hippocampal synapses.

RESULTS

Nanoscope Topography of Surface GluN1-, GluN2A-, and GluN2B-NMDARs

In order to map all membrane NMDARs, the GluN1 subunit was labeled in live hippocampal neurons at day *in vitro* (DIV) 17 using an antibody directed against the extracellular N terminus (Lü et al., 2017). Using conventional, diffraction-limited epifluorescence imaging, the classical distribution of GluN1-NMDAR clusters was observed along dendrites (Figure 1A, upper panels). In contrast, dSTORM super-resolution imaging revealed that GluN1-NMDAR clusters were composed of several adjacent nano-sized objects, which we chose to refer to as nanodomains (Figure 1A, lower panel). As NMDARs in hippocampal neurons contain GluN2A and/or GluN2B subunits, we then labeled live neurons at DIV 17 using specific custom-made antibodies directed against the extracellular N termini of GluN2A or GluN2B subunits (Figure S1). Both GluN2A- and GluN2B-NMDARs were expressed on the neuronal surface (Figures 1B and S2A). Diffraction-limited epifluorescence images of surface GluN2A- or GluN2B-NMDARs revealed comparable distributions along dendrites, with indistinguishable GluN2A- and GluN2B-NMDAR clusters (Figures 1B and S2A–S2C). Quantitative dSTORM imaging was then used to unveil the nanoscopic distribution of surface GluN2A- and GluN2B-NMDAR clusters (Figures 1B–1C and S3). Details on number of cells and independent experiments and statistical p values can be found in Table S1. In contrast with diffraction-limited epifluorescence imaging, the nanoscale distributions of GluN2A- and GluN2B-NMDARs were different at first sight, with more nanodomains of GluN2A-NMDARs. We used three gold-standard quantification approaches to analyze

Figure 1. Nano-organization of GluN2A- and GluN2B-NMDARs in Hippocampal Neurons

- (A) Live immunostaining of endogenous surface GluN1 at DIV 17 labeled with a specific custom-made antibody. Upper panels: epifluorescence images of GluN1. Left: dendritic shafts reveal a clustered distribution (scale bar, 10 μ m). Right: enlarged image of GluN1 clusters (scale bar, 500 nm). Lower panel: SR-Tesseler-segmented GluN1 cluster.
- (B) Comparison between epifluorescence (left) and super-resolution dSTORM images generated by the Leica LAS software (right) of a single dendrite stained for either GluN2A- (top) or GluN2B- (bottom) NMDARs. Dotted line represents the dendrite border based on the epifluorescence image. Scale bar, 1 μ m.
- (C) Comparison of enlarged epifluorescence and dSTORM (generated by Leica LAS software) clusters of GluN2A- (top) or GluN2B- (bottom) NMDARs. Dotted line represents the cluster border based on the epifluorescence image. Scale bar, 300 nm.
- (D) DBSCAN analysis of NMDAR clusters. Images of single GluN2A- and GluN2B-NMDAR clusters generated by LAMA software during DBSCAN analysis. Scale bar, 200 nm.
- (E) Differences in the area of super-resolved GluN2A- and GluN2B-NMDAR clusters represented by the mean \pm SEM values (DBSCAN analysis).
- (F) Wavelet-based morphometric analysis (MIA, multi-dimensional image analysis) of NMDAR nanodomains. Enlarged single cluster of GluN2A- (left, blue) or GluN2B- (right, orange) NMDARs, both composed of nanodomains. Images are representations of the MIA processing. Dotted line represents the outline of the epifluorescence cluster; arrows point to nanodomains within. Scale bar, 100 nm.
- (G) Comparison between GluN2A- and GluN2B-NMDAR nanodomains (MIA). Left: mean \pm SEM values of GluN2A- and GluN2B-NMDAR nanodomain areas. Right: mean \pm SEM values of the number of nanodomains per GluN2A- or GluN2B-NMDAR cluster.
- (H) SR-Tesseler analysis. Enlarged clusters of GluN2A- (top) and GluN2B-NMDAR generated by SR-Tesseler. Arrows point to nanodomains within the clusters. Scale bar, 100 nm.
- (I) Comparison between GluN2A- and GluN2B-NMDAR clusters and nanodomains using SR-Tesseler. Top: mean \pm SEM values of GluN2A- and GluN2B-NMDAR cluster area. Bottom left: mean \pm SEM values of GluN2A- and GluN2B-NMDAR nanodomain areas. Bottom right: mean \pm SEM values of GluN2A- and GluN2B-NMDAR nanodomain number per cluster. For statistical details, refer to Table S1. For distribution representations, see Figure S4.

and compare GluN2A- and GluN2B-NMDAR clusters (for details, refer to [STAR Methods](#)). Density-based spatial clustering of applications with noise analysis (DBSCAN) was first used to characterize the clusters ([Figure 1D](#)). The GluN2A-NMDAR nanoscale cluster area was found to be ~50% larger than that of GluN2B-NMDARs ([Figures 1E and S4A](#)), indicating that GluN2A- and GluN2B-NMDAR synaptic organizations are different. dSTORM images also revealed that these clusters were not uniform but contained distinct nanodomains ([Figure 1F](#)). In order to better characterize the intracluster organization and overcome the limitation of DBSCAN when analyzing structures in close proximity, we used a wavelet-based segmentation method applied to the intensity-based images ([Nair et al., 2013](#)) to perform a precise morphometric analysis of the nanodomains, such as the area, the number per cluster, and the shape ([Figures 1F and 1G](#)). The areas of GluN2A- and GluN2B-NMDAR nanodomains were similar ([Figures 1G and S4B](#)). However, the number of GluN2A-NMDAR nanodomains was twice as large as that of GluN2B-NMDARs ([Figures 1G and S4C](#)). Furthermore, GluN2B-NMDAR nanodomains tended to be more elongated than GluN2A-NMDAR ones as evaluated by the shape factor ([Figure S4D](#)). Thus, GluN2A- and GluN2B-NMDARs form nanodomains with subunit-specific characteristics. Additionally, this morphometric analysis approach confirmed the difference between GluN2A- and GluN2B-NMDAR clusters observed using the DBSCAN analysis ([Figure S4E](#); GluN2A: $n = 315$ clusters from 16 cells in a total number of 6 experiments; GluN2B: $n = 148$ clusters from 14 cells in a total number of 7 experiments). Finally, we used a Voronoi tessellation analysis (SR-Tesseler; segmentation framework based) to finely characterize nanodomains ([Figure 1H](#)) ([Levet et al., 2015](#)). Consistent with the previous analysis methods, GluN2A-NMDAR cluster area was found to be 50% larger than that of GluN2B-NMDARs ([Figures 1I and S4F](#); for both GluN2A and GluN2B: $n = 91$ clusters from 8 cells in a total number of 4 experiments). In addition, GluN2A- and GluN2B-NMDAR nanodomain areas were similar, whereas their numbers were different ([Figures 1I, S4G, and S4H](#)). We further validated these 2D quantifications by performing 3D dSTORM imaging of both NMDAR subtypes using the SELF1 method to achieve quasi-isotropic 3D resolution independently of optical aberrations induced by sample inhomogeneities ([Bon et al., 2018](#)) and confirmed that the nano-organizations of GluN2A- and GluN2B-NMDARs were different, especially in terms of the nanodomain number per cluster ([Figure S5](#)). Thus, both GluN2A- and GluN2B-NMDARs are differentially organized in surface clusters.

Although most surface NMDAR clusters are synaptic ([Figure S6](#)), we then specifically investigated the nanoscale organization of GluN2A- and GluN2B-NMDARs within glutamatergic synapses labeled with the postsynaptic marker PSD95. GluN2A-NMDAR clusters were more strongly colocalized with PSD95 than GluN2B-NMDARs ([Figures S7A and S7B](#)). When their synaptic organization was compared at the nanoscale level, the number and area of synaptic (PSD95-positive) GluN2A-NMDAR nanodomains were found to be larger than that of GluN2B-NMDARs ([Figures S7C–S7G](#)), consistent with previous observations. Noteworthy, fewer GluN2A- and GluN2B-NMDAR nanodomains were found when comparing non-synaptic (immu-

nonegative for PSD95) to synaptic clusters (nanodomain number: GluN2A, PSD95+: 5.6 ± 0.25 , $n = 186$; PSD95–: 3.4 ± 0.3 , $n = 128$ clusters; $p < 0.001$; GluN2B, PSD95+: 2.9 ± 0.2 , $n = 69$; PSD95–: 1.7 ± 0.1 , $n = 68$ clusters; $p < 0.001$). Collectively, these data indicate that GluN2A- and GluN2B-NMDAR clusters are organized in nanoscale objects that bear subtype-specific features, particularly at synaptic sites.

Comparative Nanoscale Organization of GluN2A- and GluN2B-NMDARs within a Same Synapse

The differential nanoscale organization of GluN2A- and GluN2B-NMDARs suggests that these subtypes are not confined into similar compartments, even though GluN2A and GluN2B clusters appear to fully overlap in diffraction-limited images ([Figure S8](#)). To test this assumption, we decided to label simultaneously GluN2A- and GluN2B-NMDARs within synaptic GluN1-NMDAR clusters ([Figure S6](#)). To this end, we co-expressed exogenous GluN2A-HA and GluN2B-FLAG, as well as GluN1-GFP, to delineate NMDAR clusters within dendritic spines ([Figure 2A](#)). The nanoscale organization of GluN2A- and GluN2B-NMDARs within the same GluN1-NMDAR clusters was similar to the one described in distinct clusters (e.g., number of nanodomains per cluster: 2.8 ± 0.3 GluN2A-HA, 1.4 ± 0.17 GluN2B-Flag, Mann Whitney test $p < 0.0001$) ([Figure 2B](#)). Interestingly, most GluN2A- and GluN2B-NMDAR nanodomains did not overlap with each other ([Figures 2B and 2C](#)). Indeed, the colocalization between nanodomains, measured as the fraction of overlapping surface divided by the total surface of the nanodomains of each label, only ranged between 20% and 40% ([Figure 2D](#)). This suggests that only a limited fraction of receptor subtypes are intermixed. Finally, we used two-color stimulated emission depletion (STED) microscopy, a conceptually different super-resolution imaging technique, to further decipher the nanoscale organization of tagged GluN2A- and GluN2B-NMDARs in the same GluN1-NMDAR cluster. Two-color STED images confirmed a heterogeneous distribution of each receptor subtype, and the larger area occupied by GluN2A-NMDAR clusters compared to GluN2B-NMDARs ([Figures S9A and S9B](#)). Furthermore, only 30% of GluN2A-NMDARs were found to overlap with GluN2B-NMDARs in a given cluster ([Figure S9C](#)). Collectively, these data demonstrate that, at a given synapse, GluN2A- and GluN2B-NMDAR nanoscale organizations are different, and their respective nanodomains do not overlap extensively.

Developmental Changes in the Nano-organization of GluN2A- and GluN2B-NMDARs

During brain development, the subunit composition of NMDARs changes (e.g., [Barth and Malenka, 2001](#); [Monyer et al., 1994](#)). In rodents, GluN2B-NMDARs are highly expressed at immature synapses, whereas GluN2A-NMDAR synaptic levels increase progressively after birth. To understand the nanoscale maturation of GluN2A- and GluN2B-NMDARs and explore whether the differences in GluN2A-/GluN2B-NMDAR nano-organization persist throughout development, we immunostained these receptor subtypes at different time points of cell culture maturation. First, we established the maturation profile of glutamatergic synapses (PSD95+) in our cultured hippocampal networks, confirming that synapse numbers increase significantly over two

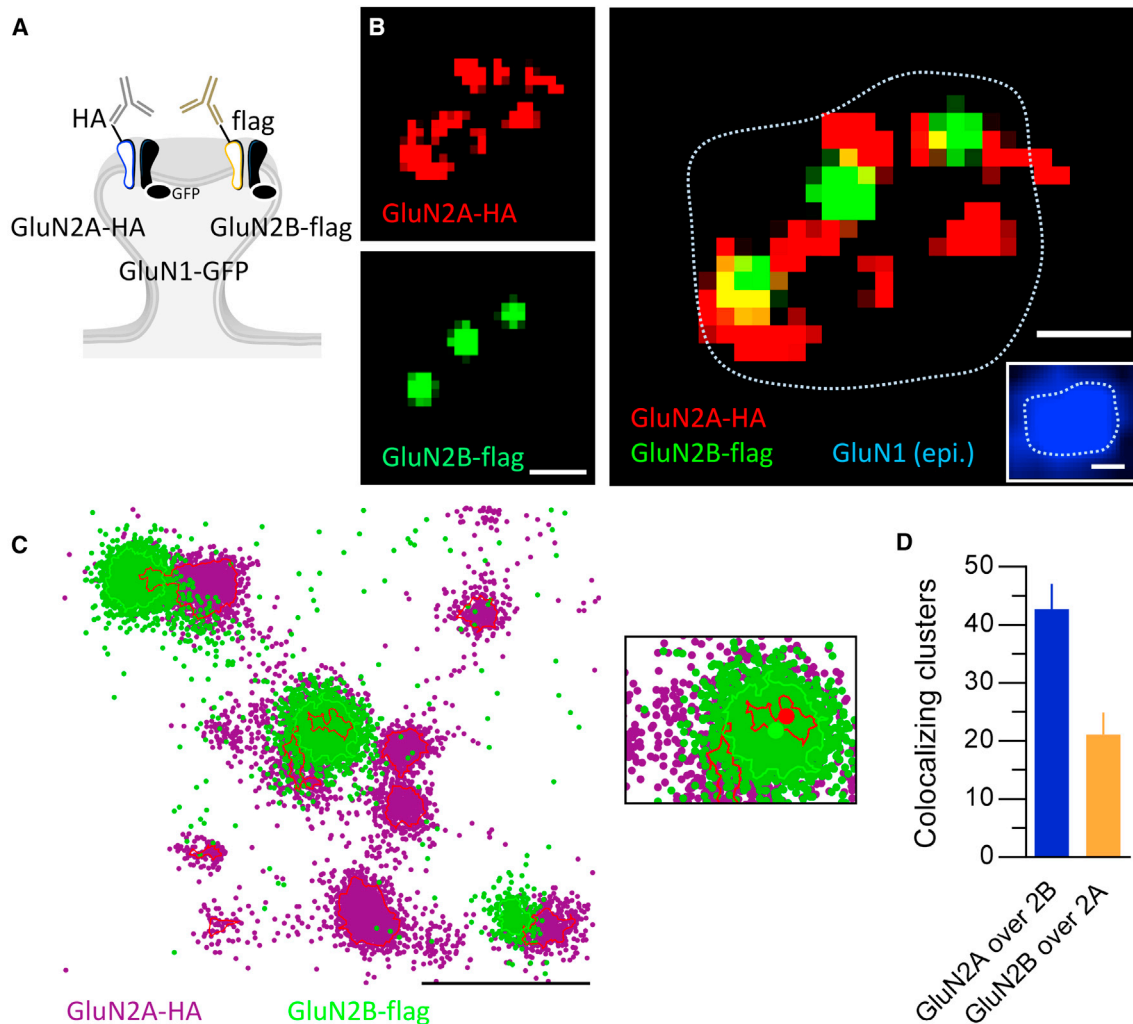


Figure 2. Comparative Nano-organization of GluN2A- and GluN2B-NMDAR within the Same Synaptic Compartment

(A) Schematic representation of experimental design. Hippocampal neurons were co-transfected with GluN1-GFP, GluN2A-HA, and GluN2B-FLAG at DIV 10. The extracellularly expressed HA- and FLAG tags were used to label GluN2A- and GluN2B-NMDARs, respectively, after 4 days of expression.

(B) Two-color dSTORM image of GluN2A-HA (red) and GluN2B-FLAG (green). The dotted outline represents the outline of the GluN1-GFP epifluorescence cluster (lower inset; scale bar, 150 nm). Scale bar, 100 nm.

(C) SR-Tesseler images of two-color dSTORM of GluN2A-HA (magenta) and GluN2B-FLAG (green). Right inset: enlarged view of clusters in which the barycenters are indicated by dots. The red and green lines indicate the borders of GluN2A- and GluN2B-NMDAR nanodomains, respectively. Scale bar, 100 nm.

(D) Percentage of colocalization between GluN2A-HA and GluN2B-FLAG represented by mean \pm SEM values obtained by SR-Tesseler.

weeks *in vitro* and show a concomitant developmental switch in GluN2A/B subunit enrichment (Figure S2). Next, we labeled GluN2A- or GluN2B-NMDARs in live neurons at DIV 10, 17, or 24 to perform dSTORM imaging. Interestingly, GluN2A-NMDAR clusters underwent a major reorganization throughout development (Figures 3A–3F). Indeed, all cluster parameters—including area, molecule numbers, and nanodomain area and numbers per cluster—were affected (Figures 3A–3F), with a marked change at DIV 17, a developmental stage at which most glutamatergic synapses acquire the axon-spine morphology. On average, GluN2A-NMDAR cluster areas increased between DIV 10 and 17, then diminished at DIV 24 (Figure 3B). These changes were paralleled by changes in the molecule density per cluster (Fig-

ure 3C), as well as in the absolute number of molecules (Table S2). For GluN2B-NMDAR clusters, only subtle changes were observed during this period (Figures 3A–3F). GluN2B-NMDAR cluster areas increased between DIV 10 to 17, then remained stable over time (Figure 3B). The molecule density per GluN2B-NMDAR cluster and the absolute number of molecules (Table S2) were not correlated with this profile, as it was highest at immature states, decreasing during maturation (Figure 3C). When comparing both NMDAR subtypes over these developmental stages, the GluN2A-NMDAR cluster area was found to be initially larger at DIVs 10 and 17 compared to GluN2B-NMDARs, but this difference did not persist at DIV 24 (Figure 3B). Thus, the maturation profiles of GluN2A- and

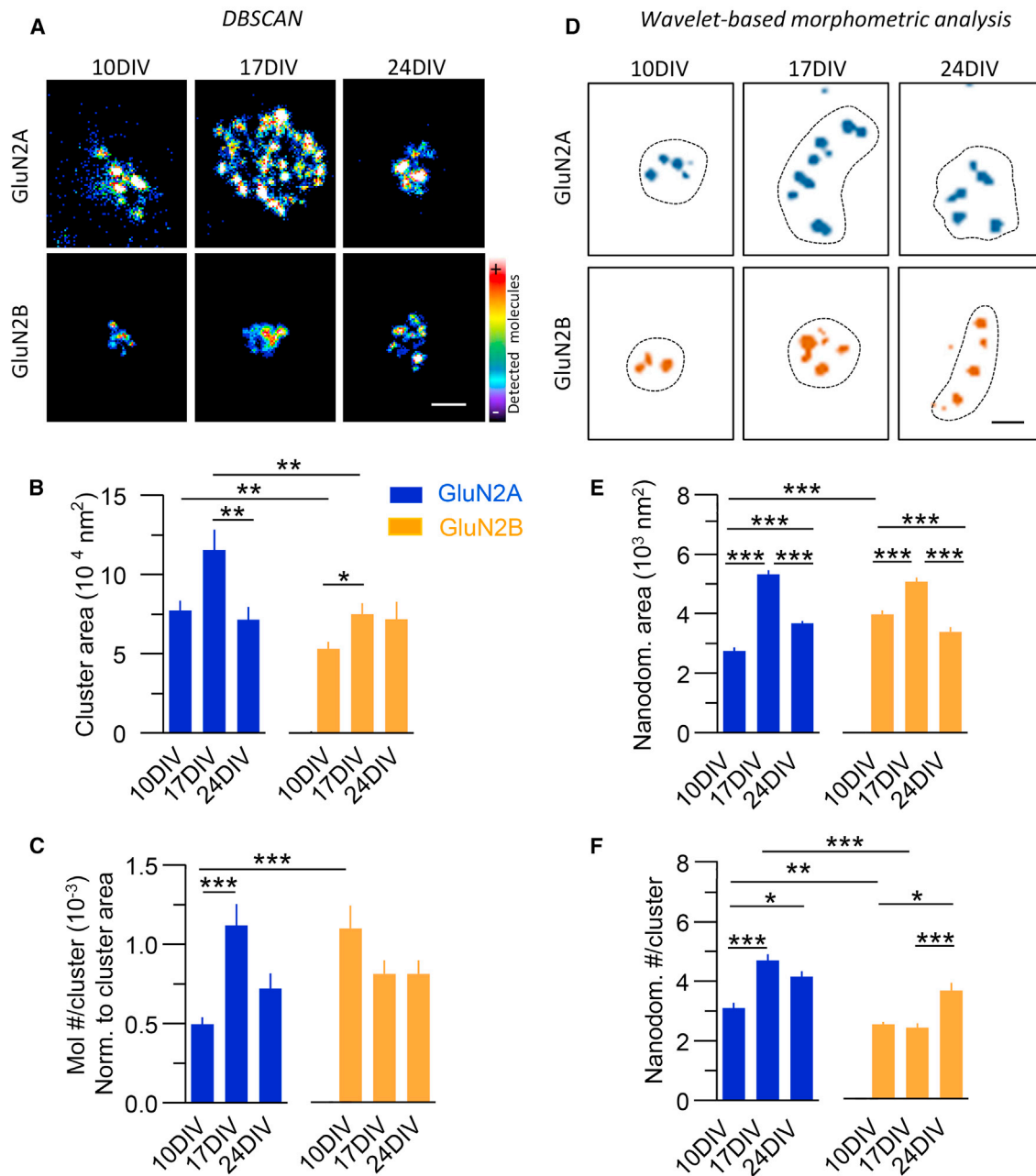


Figure 3. Nanoscopic Reorganization of GluN2A- and GluN2B-NMDARs during Development

(A) Images of enlarged clusters of GluN2A- (top) or GluN2B- (bottom) NMDARs during development of neuronal cultures. Images were generated by Lama software. Scale bar, 200 nm.

(B) Changes in the cluster area of GluN2A- or GluN2B-NMDARs during development.

(C) Developmental changes in the molecule number per GluN2A- and GluN2B-NMDAR cluster. Values are normalized to cluster area. For absolute numbers, see Table S2.

(D) Developmental changes in nanodomains within GluN2A- (top) and GluN2B- (bottom) NMDAR clusters (MIA). The dotted line represents the outline of respective epifluorescence clusters. Scale bar, 100 nm.

(E) Developmental changes in the area of GluN2A- and GluN2B-NMDAR nanodomains.

(F) Developmental changes in the number of nanodomains per cluster of GluN2A- or GluN2B-NMDARs. For statistical details, refer to Table S1.

GluN2B-NMDAR nanoscale organizations were different. When exploring the evolution of morphometric characteristics of GluN2A- and GluN2B-NMDAR nanodomains over this develop-

mental period, a similar trend was observed. Although initially larger for GluN2B-NMDAR compared to GluN2A-NMDAR at DIV 10, the nanodomain areas of both NMDAR subtypes

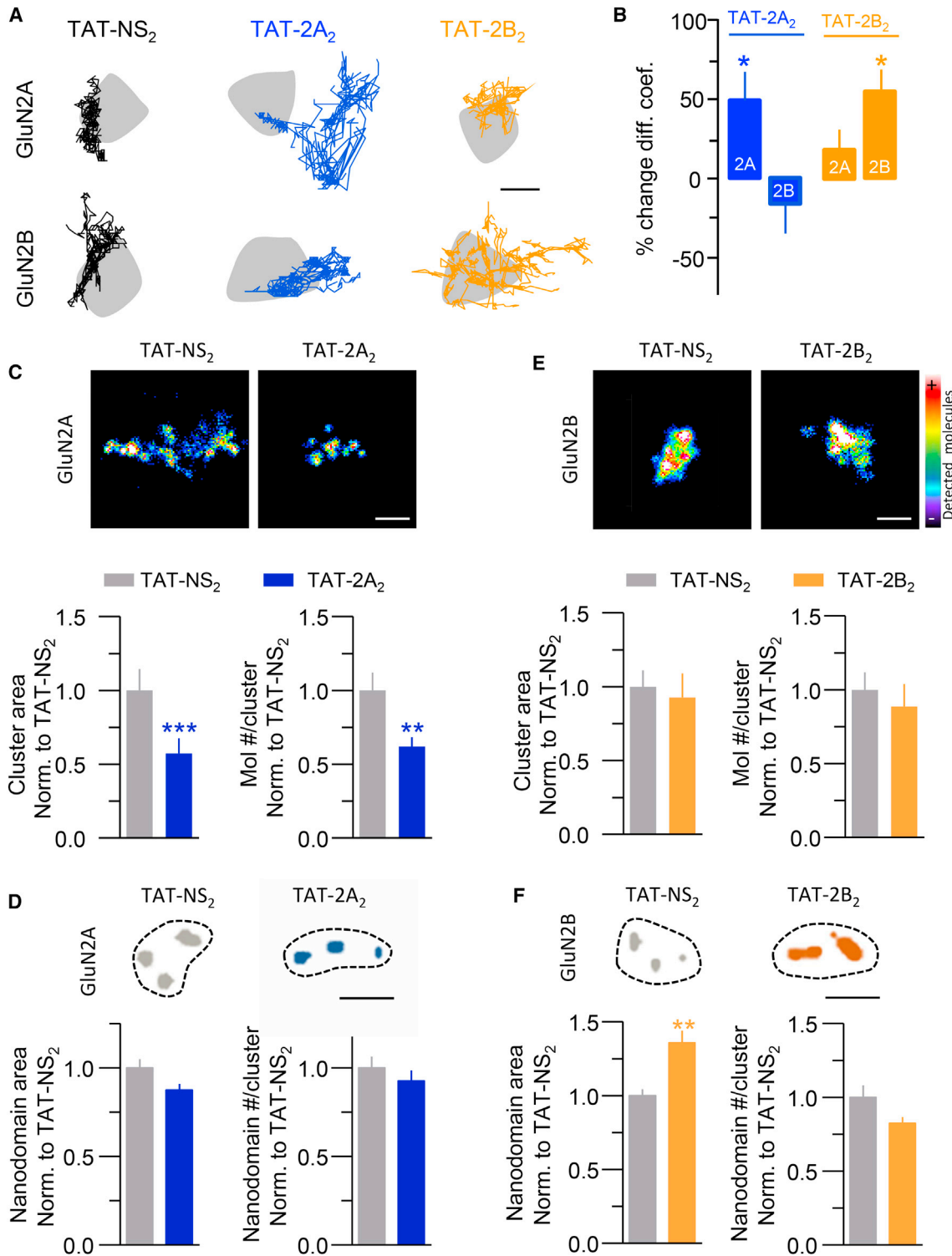


Figure 4. Selective Reorganization of GluN2A- and GluN2B-NMDARs using Biomimetic Ligands

(A and B) Effects of TAT-conjugated competing ligands on GluN2A- and GluN2B-NMDAR surface trafficking within synapses.

(A) Single-nanoparticle (quantum dot) trajectories of GluN2A- and GluN2B-NMDARs in presence of either TAT-NS₂, TAT-2A₂, or TAT-2B₂ ligands (mimicking the last 15 amino acids of either GluN2A or GluN2B subunit C termini). The synaptic area was defined by Mitotracker staining (see STAR Methods). Scale bar, 150 nm.

(B) Percent change in instantaneous synaptic diffusion coefficients of GluN2A- and GluN2B-QD complexes exposed to either TAT-NS₂, TAT-2A₂, or TAT-2B₂ ligands. The values are expressed as percent of variation to the TAT-NS₂ condition.

(legend continued on next page)

followed a comparable maturation profile changing after 2 weeks in culture (Figure 3E). No significant difference was later observed at DIV24. The number of nanodomains also increased at DIV 17 for GluN2A-NMDAR, whereas for GluN2B-NMDAR, it increased only at later stages (Figure 3F), although GluN2A-NMDAR clusters contained more nanodomains compared to GluN2B-NMDARs at all maturation stages. Together, these data indicate that the nanoscale organization of GluN2A- and GluN2B-NMDARs is highly regulated throughout the *in vitro* maturation of hippocampal networks and suggest the presence of distinct regulatory strategies for each receptor subtype.

PDZ Scaffold Differentially Regulates NMDAR Nanoscale Organization

To directly test whether different cellular mechanisms regulate the nanoscale organization of GluN2A- and GluN2B-NMDARs, we probed each subtype by interfering with its synaptic anchoring (Lau and Zukin, 2007). The PDZ binding motif at the C termini of GluN2A- and GluN2B-NMDARs is involved in interaction with membrane-associated guanylate kinases (MAGUKs) and plays a critical role in the synaptic organization of NMDARs (Frank et al., 2016). Thus, we chose to selectively alter GluN2A or GluN2B interactions with PDZ scaffolds using divalent biomimetic competing ligands that were applied for tens of minutes only in order to avoid any potential long-term synaptic re-organizations (Figure S10) (Bard et al., 2010; Sainlos et al., 2011). Building up on previously described peptides derived from the GluN2A subunit (Bard et al., 2010), we also designed ligands that mimic the GluN2B C-terminal motifs. Comparably to the GluN2A-derived divalent ligands, the GluN2B-based divalent biomimetic peptides showed an improved capacity to bind PDZ domains clusters over their corresponding monovalent counterparts (Figures S10, S11, and S12). To quantify the capacity of biomimetic divalent competitive ligands to destabilize subunits in live synapses, single-nanoparticle (quantum dot) tracking of GluN2A or GluN2B subunits was performed in neurons acutely exposed to cell-permeant TAT-conjugated peptides. Consistent with previous studies (Bard et al., 2010; Sainlos et al., 2011), competitive ligands strongly, selectively, and similarly interfered with the binding of the C-terminal domain of either GluN2A or GluN2B subunits with PDZ scaffold proteins (Figures 4A and 4B). In the presence of TAT-2A₂ ligands, the cluster area and molecule number of GluN2A-NMDARs were decreased significantly (Figure 4C and Table S2). As the nanodomain area and number remained stable (Figure 4D), the relative density of GluN2A-NMDARs within nanodomains significantly decreased (Figure S13A). In this condition, a slight but significant change in the GluN2B-NMDAR nanoscale organization was observed—i.e., an increased num-

ber of nanodomains (Figure S14A–S14D). Thus, when the interaction between GluN2A-NMDARs and PDZ scaffolds is artificially disrupted, GluN2A-NMDAR nanodomains are partially depleted in receptors, while their geometry remains stable, and a mild simultaneous redistribution of GluN2B-NMDAR is observed.

Surprisingly, when GluN2B-NMDARs were challenged with TAT-2B₂ ligands, their nanoscale cluster area and molecule number were unaltered (Figure 4E and Table S2). Instead, the area of nanodomains significantly increased (Figure 4F), leading to a decrease in receptor density within nanodomains (Figure S13B). In parallel, a slight—but significant—change in the GluN2A-NMDAR nanoscale organization was observed (Figure S14E–S14H). Thus, disrupting the interaction between GluN2B-NMDARs and PDZ scaffolds triggers their redistribution within the synapse, promoting a reorganization of nanodomains without affecting receptor numbers. Together, these data demonstrate that GluN2A- and GluN2B-NMDARs are differentially regulated by the binding to PDZ scaffold. The regulation of GluN2A-NMDARs would thus involve changes in the receptor pool within stably defined nanodomains, whereas the regulation of GluN2B-NMDARs involves changes in the nanodomain topography with a rather stable receptor pool.

GluN2A- and GluN2B-NMDAR Nanoscale Redistributions Tune Synaptic LTP

The observation that GluN2A- and GluN2B-NMDAR nanoscale organizations are distinct and differentially regulated by scaffold partners raises the possibility that these nanodomains are involved in different physiological functions. Earlier studies have revealed that both GluN2A- and GluN2B-subunit-containing NMDARs are involved in long-term synaptic plasticity (Shipton and Paulsen, 2013; Yashiro and Philpot, 2008). However, the respective contribution of each receptor subtype to synaptic LTP is still hotly disputed, mainly because of the limitations inherent to the antagonist- or knockout-based approaches involved. To circumvent this, we took advantage of the biomimetic competing ligands described above aiming to selectively disorganize either GluN2A- or GluN2B-NMDAR synaptic nanodomains and to see how this affects LTP expression.

First, we examined the relative synaptic content of GluN2A- and GluN2B-NMDARs by recording NMDAR-mediated excitatory postsynaptic currents (EPSCs) at CA3-CA1 glutamatergic synapses in presence of either NS₂, 2A₂, or 2B₂ ligands infused through the patch pipette while delivering bath applications of the GluN2A- or the GluN2B-selective antagonists Zn²⁺ (250 nM) and Ro 25-6981 (2 μM), respectively (Figure 5). In the absence of biomimetic peptide or in the presence of the control NS₂ ligand, a significant decrease in NMDAR EPSC amplitude was observed

(C) Top: enlarged GluN2A-NMDAR cluster (Lama) following stimulation with either TAT-NS₂ or specific TAT-2A₂ ligands. Scale bar, 200 nm. Bottom: mean ± SEM values of GluN2A-NMDAR cluster area and molecule number per cluster in control and TAT-2A₂ ligand conditions. Values are normalized to TAT-NS₂.

(D) Top: GluN2A-NMDAR nanodomains (MIA) following treatment with either TAT-NS₂ or specific TAT-2A₂ ligands. Dotted line represents the outline of respective epifluorescence clusters. Scale bar, 200 nm. Bottom: mean ± SEM values of GluN2A-NMDAR nanodomain area and number per cluster.

(E) Top: enlarged GluN2B-NMDAR cluster (Lama) following stimulation with either TAT-NS₂ or specific TAT-2B₂ ligands. Scale bar, 200 nm. Bottom: mean ± SEM values of GluN2B-NMDAR cluster area and molecule number per cluster in control and TAT-2B₂ conditions. Values are normalized to TAT-NS₂.

(F) Top: GluN2B-NMDAR nanodomains (MIA) following treatment with either TAT-NS₂ or specific TAT-2B₂ ligands. Dotted line represents the outline of respective epifluorescence clusters. Scale bar, 200 nm. Bottom: mean ± SEM values of GluN2B-NMDAR nanodomain area and number per cluster. Scale bar, 200 nm. For statistical details, refer to Table S1.

in presence of Ro 25-6981 (by 27% or 32%, respectively; [Figures 5A–5C](#)). This reflected the basal GluN2B-NMDAR contribution to NMDAR-mediated synaptic currents. Conversely, partial GluN2A blockade through Zn^{2+} (250 nM) application inhibited NMDAR-mediated EPSCs by 41% in the absence of peptide and by 36% in the presence of the control NS_2 ligand ([Figures 5D–5F](#)). In comparison, $2A_2$ ligand infusion enhanced the Ro 25-6981-dependent inhibition of NMDAR EPSC by up to 43% and decreased Zn^{2+} -dependent NMDAR blockade down to 16%, consistent with a lateral escape of synaptic GluN2A-NMDARs and relative enrichment in GluN2B-NMDARs ([Figures 5A–5F](#)). When infusing the $2B_2$ ligand, Ro 25-6981-dependent inhibition of NMDAR EPSC significantly decreased down to 12% while Zn^{2+} -dependent blockade increased up to 60%, consistent with a synaptic depletion of GluN2B-NMDARs and a relative enrichment in GluN2A-NMDARs ([Figures 5A–5F](#)). Interestingly, these manipulations only altered the relative abundance of GluN2A- and GluN2B-NMDARs as the overall amount of synaptic NMDARs remained stable. Indeed, the amplitude of NMDAR EPSCs at CA3-CA1 glutamatergic synapses was unchanged during the exposure to either NS_2 , $2A_2$, or $2B_2$ ligands ([Figures 5G and 5H](#)), consistent with earlier observations in cultured hippocampal neurons ([Bard et al., 2010](#)). Thus, these competing ligands alter the receptor nanoscale organization and GluN2A/2B synaptic ratio (20%–40%), but leave the overall amplitude of NMDAR-mediated currents intact.

We next tested the role of GluN2A- and GluN2B-NMDAR relative organization in the ability of CA3-CA1 synapses to express LTP. A standard LTP-induction protocol with NS_2 control ligands infused whole cell produced a persistent 214% potentiation that could be fully blocked by the bath application of the NMDAR competitive antagonist AP5 (50 μ M) ([Figures 6A–6C](#)). Strikingly, whole-cell dialysis of $2A_2$ increased the magnitude of LTP (measured 40 min after induction) by 64% when compared to the control NS_2 ligand infusion condition ([Figures 6A–6C](#)). In contrast, $2B_2$ dialysis decreased the magnitude of LTP by 86% when compared to the NS_2 condition ([Figures 6A–6C](#)). Collectively, these data suggest that the acute manipulation of the GluN2A/GluN2B-NMDAR synaptic ratio, while having no effect on the overall NMDAR-mediated synaptic current, bi-directionally controls the range of use-dependent plasticity at CA3-CA1 hippocampal synapses: depleting synapses in GluN2A-NMDARs strengthens LTP expression, whereas increasing the contribution of GluN2A-NMDARs weakens it.

DISCUSSION

Here, we used SMLM imaging and patch-clamp electrophysiology in hippocampal neurons to reveal the nanoscale organization of GluN2A- and GluN2B-NMDARs and its functional role in synaptic plasticity. Documenting the distribution of individual molecules revealed substantial differences between the nanoscale structures of the two NMDAR subtypes, particularly in the number, area, and shape of their nanodomains. At a given synapse, only a fraction of GluN2A- and GluN2B-NMDAR nanodomains overlap, indicating the presence of distinct regulatory macromolecular complexes that differentially evolve during development. Remarkably, acute exogenous re-organization of GluN2A- and GluN2B-

NMDARs, which leaves intact the overall NMDAR-mediated current, bi-directionally tunes synaptic LTP ([Figure 6D](#)). Thus, the nanoscale organizations of membrane GluN2A- and GluN2B-NMDARs in hippocampal neurons are structurally different, regulated through distinct cellular mechanisms, and have contrasted consequences on the plastic range of synapses.

Advances in super-resolution microscopy have revealed that the nanoscale organization of neurotransmitter receptors, scaffolds, and signaling molecules is structured in the postsynaptic compartment ([Broadhead et al., 2016; Frost et al., 2010; MacGillavry et al., 2013; Nair et al., 2013](#)). For instance, in hippocampal synapses, AMPA receptors and PSD95 are clustered in 1–4 nanodomains (\sim 50–80 nm size) that have been proposed to be plastic entities ([MacGillavry et al., 2013; Nair et al., 2013](#)). A subtype specificity in the nanoscale distribution of surface and intracellular GluN2A/2B-NMDAR was previously suggested based on the differential enrichment in PSD95 clusters ([MacGillavry et al., 2013](#)). Here, we provide the first surface mapping of both GluN2A- and GluN2B-NMDARs at the nanoscale level, revealing the presence of approximately 5–10 nanodomains (\sim 55 nm) per synaptic area. The similarities between AMPA receptors, PSD95, and now NMDAR nanodomains in hippocampal synapses strengthen the view that the postsynaptic region is a highly compartmentalized entity. Interestingly, nanoclusters have also been identified with respect to other, non-neuronal membrane proteins ([Garcia-Parajo et al., 2014](#)). Therefore, nanoclustering appears to be a dominant feature of membrane protein organization which potentially represents a mode of spatiotemporal orchestration of biochemical reactions as suggested by liquid-liquid phase transitions ([Li et al., 2012](#)). Compartmentalization is even more critical for the postsynaptic terminal in which it can accelerate reaction kinetics for signal transmission, as for PSD95 and SynGAP ([Zeng et al., 2016](#)). The postsynaptic receptor nanodomains are likely to boost neurotransmitter signals as they are spatially juxtaposed to the presynaptic release machinery ([Tang et al., 2016](#)). The differential and largely non-overlapping nanoscale organization of GluN2A- and GluN2B-NMDARs described here thus suggests the presence of distinct NMDAR-mediated transmission units. Furthermore, our data indicate that, if present, the GluN2A/2B tri-heterotetramers ([Al-Hallaq et al., 2007; Gray et al., 2011; Rauer and Köhr, 2011](#)) could represent up to 30% of postsynaptic NMDARs. Thus, NMDAR signaling may proceed from a nanoscale mosaic of GluN2A- and GluN2B-NMDAR complexes that could constitute, or be part of, distinct functional units in the synapse.

Over the past few decades, the mechanisms underlying the trafficking and synaptic anchoring of GluN2A- and GluN2B-NMDARs have been the subject of intense investigations. It has been proposed that the binding of GluN2A/B subunits to different MAGUK proteins, through the interaction between the C terminus of GluN2A/2B subunits and PDZ domain of MAGUKs, plays an important role in their synaptic anchoring ([Horak et al., 2014; Lussier et al., 2015](#)). Here, surface GluN2A- and GluN2B-NMDARs were acutely challenged with high-affinity competing ligand, and their surface reorganization was monitored at the single-molecule and nanoscale levels. Although such competing ligands can theoretically interfere with other

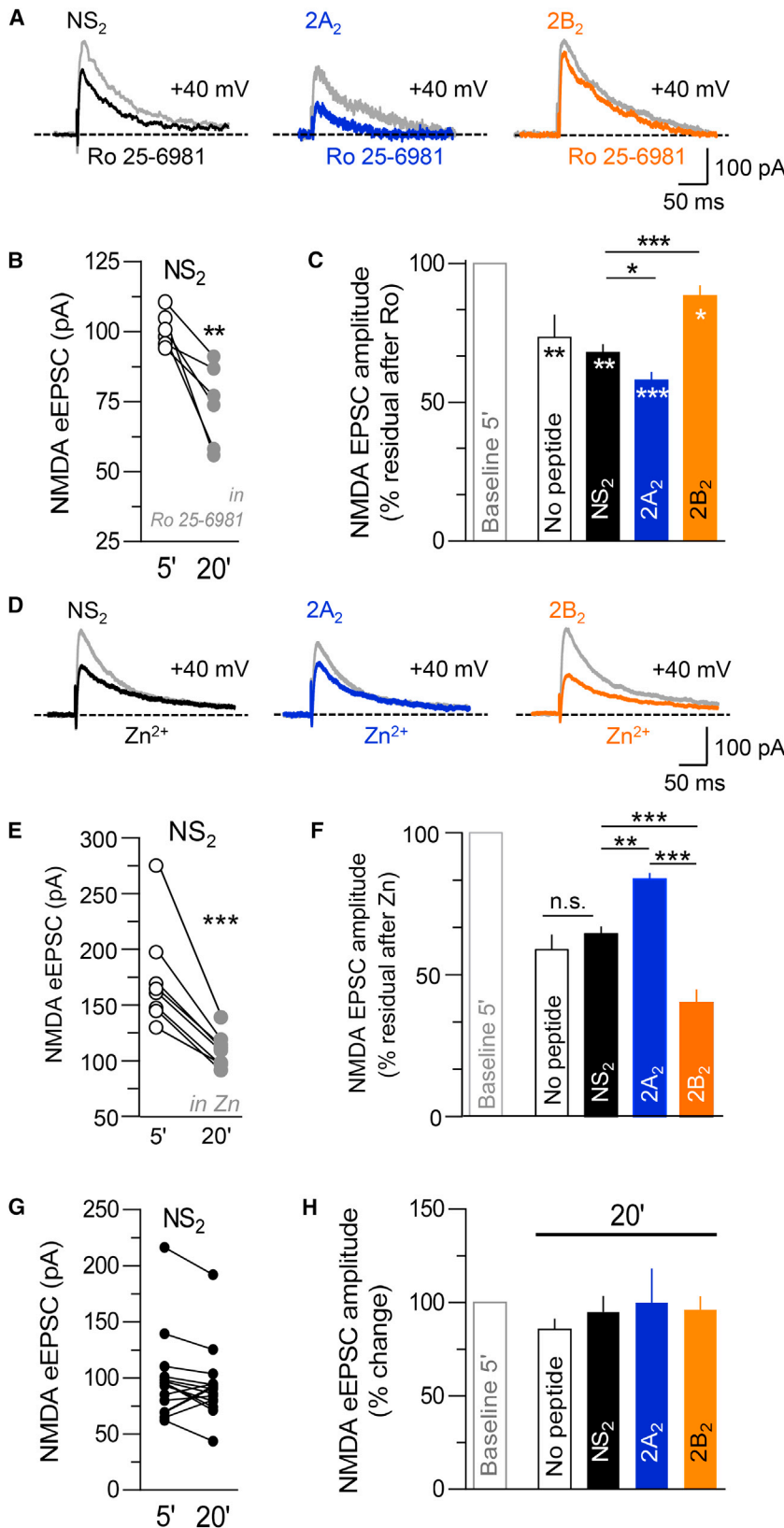


Figure 5. Selective Disruption of the Interaction between GluN2A- or GluN2B-NMDARs and PDZ Proteins Allows Acute Manipulation of the Composition of Synaptic NMDAR

(A) Representative NMDAR-mediated EPSC traces recorded at CA3-CA1 synapses from P17 to P22 C57bl6j mice before and after incubation with Ro 25-6981 (2 μ M) in the presence of either non-sense (NS₂; black), GluN2A-selective (2A₂; blue), or GluN2B-selective (2B₂; orange) competing ligands (5 μ M) infused through the patch pipette.

(B) NMDAR-mediated EPSC amplitude before and after incubation with Ro 25-6981 (2 μ M) in the presence of NS₂ non-sense ligand.

(C) Relative NMDAR-mediated EPSC amplitude after 20 min incubation with Ro 25-6981 (2 μ M) in the absence or presence of non-sense (NS₂; black), GluN2A-selective (2A₂; blue), or GluN2B-selective (2B₂; orange) competing ligands (5 μ M) infused through the patch pipette.

(D) Representative NMDAR-mediated EPSC traces recorded at CA3-CA1 synapses from P17 to P22 C57bl6j mice before and after incubation with Zn²⁺ (250 nM) in the presence of either non-sense (NS₂; black), GluN2A-selective (2A₂; blue), or GluN2B-selective (2B₂; orange) competing ligands (5 μ M) infused through the patch pipette.

(E) NMDAR-mediated EPSC amplitude before and after incubation with Zn²⁺ (250 nM) in the presence of NS₂ non-sense ligand.

(F) Relative NMDAR-mediated EPSC amplitude after 20 min incubation with Zn²⁺ (250 nM) in the absence or presence of non-sense (NS₂; black), GluN2A-selective (2A₂; blue), or GluN2B-selective (2B₂; orange) competing ligands (5 μ M) infused through the patch pipette.

(G) NMDAR-mediated EPSC amplitude 5 min and 20 min after incubation with NS₂ non-sense ligand.

(H) Relative NMDAR-mediated EPSC amplitude after a 20 min exposure to non-sense (NS₂; black), GluN2A-selective (2A₂; blue), or GluN2B-selective (2B₂; orange) competing ligands (5 μ M) infused through the patch pipette.

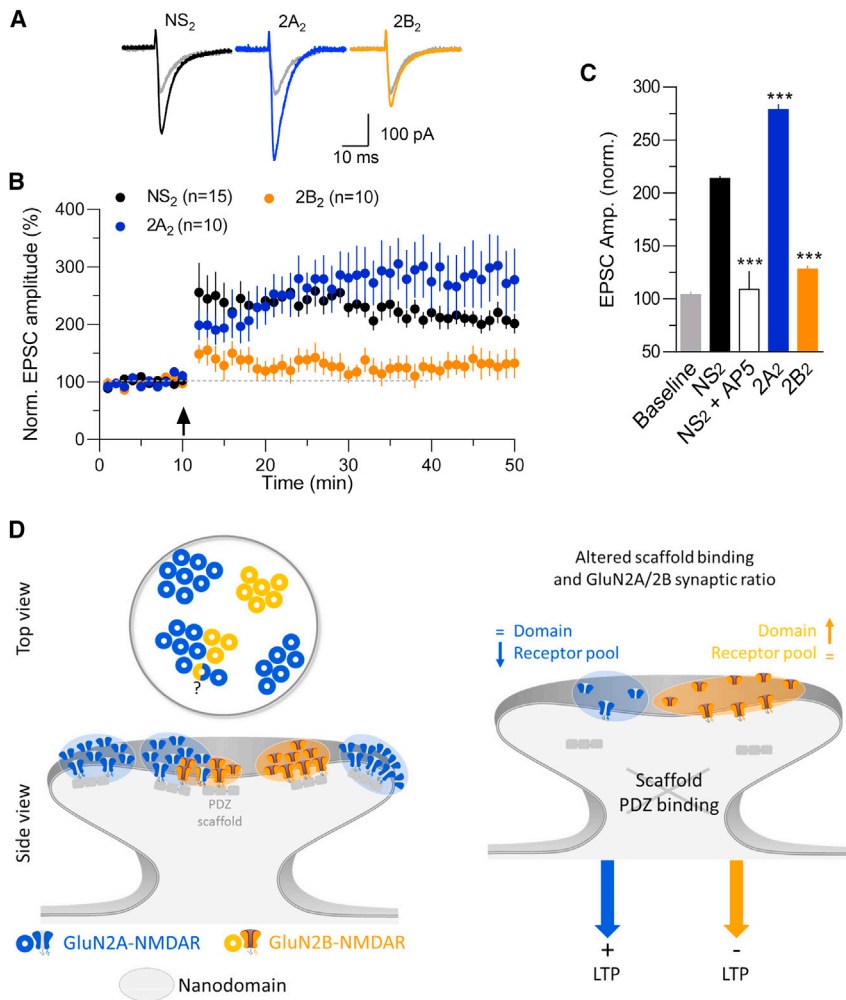


Figure 6. Acute Manipulation of the GluN2A/GluN2B-NMDAR Synaptic Ratio Bi-directionally Regulates LTP at CA3-CA1 Synapses

(A) Representative EPSC traces recorded at CA3-CA1 synapses from P17 to P22 C57Bl6j mice during baseline (gray) or 40–45 min after pairing in the presence of either non-sense (NS₂; black), GluN2A-selective (2A₂; blue), or GluN2B-selective (2B₂; orange) competing ligands (5 μM) infused through the patch pipette.

(B) Average time course of pairing-induced LTP. Normalized EPSC amplitudes (normalization to the mean amplitude of EPSCs recorded during baseline acquisition) are plotted against time for non-sense (NS₂; black), GluN2A-selective (2A₂; blue), and GluN2B-selective (2B₂; orange) competing ligands conditions. Data are presented as mean ± SEM.

(C) Normalized EPSC amplitudes at baseline or 40–45 min after pairing in non-sense (NS₂; black), non-sense + AP5 50 μM (NS₂ + AP5; white), GluN2A-selective (2A₂; blue), and GluN2B-selective (2B₂; orange) competing ligands conditions. Data are presented as mean ± SEM. Preventing the synaptic stabilization of GluN2A-NMDAR increased the plastic range of hippocampal synapses, while preventing the synaptic stabilization of GluN2B-NMDAR decreased it.

(D) In basal condition, GluN2A- and GluN2B-NMDARs are organized in nanodomains (GluN2A > GluN2B). After disrupting the interaction between C termini and PDZ scaffolds, GluN2A- and GluN2B-NMDAR nanodomains are reorganized through two distinct modes: the number of GluN2A-NMDARs is altered in a fixed domain, whereas the number of GluN2B-NMDARs remains unchanged in an altered “labile” domain. These manipulations lead to opposite changes in LTP at CA3-CA1 synapses.

PDZ domain-mediated interactions, the organization of both GluN2A- and GluN2B-NMDARs was specifically altered by these molecular challenges, which was consistent with the role of PDZ scaffolds in the regulation of NMDAR-mediated transmission (Horak et al., 2014; Lussier et al., 2015). However, these modifications differed depending on the receptor subtype considered. Preventing the interaction between GluN2A-NMDARs and PDZ scaffolds—as measured in synapses and with ligand assays—reduced the number of receptors while preserving stable nanodomain topography. In contrast, disrupting the interaction between GluN2B-NMDARs and PDZ scaffolds did not alter receptor numbers but instead affected the topography of nanodomains. These observations lend support to a model in which synapses would control GluN2A-NMDAR signaling by changing their number in defined stable domains and GluN2B-NMDAR signaling by changing their topological organization. One prediction for GluN2B-NMDAR redistribution is that once their anchoring with PDZ scaffold is disrupted, other mechanism(s) ensure their synaptic retention in different compartment(s). Furthermore, our data suggest that GluN2A- and GluN2B-NMDARs are in distinct complexes and/or domains. Consistent

with these observations, NMDARs have been proposed to be partitioned into two discrete populations *in vivo* that are referred to as 0.8 and 1.5 MDa NMDAR complexes that contain different subunit amounts and receptor combinations (Frank et al., 2016). In addition, GluN2A- and GluN2B-NMDARs do not play the same role in these complexes, as the disruption of the interaction between GluN2B-NMDARs and MAGUK proteins dismantles NMDAR supercomplexes specifically (1.5 MDa). The GluN2A and GluN2B-NMDARs are thus likely to be specifically embedded into distinct nanoscale complexes, with different signaling cascade(s) and function(s).

What is the functional significance of this subunit-specific nanoscale organization of synaptic NMDA receptors? GluN2A- and GluN2B-NMDARs have been shown to differentially influence brain development, plasticity, and sensory experience processes (Lau and Zukin, 2007; Paoletti et al., 2013). However, defining the respective roles of each receptor subtype in synaptic potentiation has remained a controversial issue, with the somewhat contrasting conclusions originating from antagonist- or knockout-based studies addressing this question. Indeed, pharmacological or genetic interventions on either subunit had a varying impact on

NMDAR-dependent LTP expression depending on the age and brain region (Shipton and Paulsen, 2013; Volianskis et al., 2015). Using divalent biomimetic ligands selectively acting on the synaptic content and nano-organization of GluN2A- or GluN2B-NMDARs, we show here that the GluN2A/2B ratio bi-directionally controls LTP at CA3-CA1 hippocampal synapses. Indeed, the 2A₂ and 2B₂ ligand infusions resulted in significant and selective up- and downregulations of GluN2A- and GluN2B-NMDAR contributions, respectively, while leaving NMDAR current amplitudes intact, suggesting that compensatory mechanisms allow for the maintenance of NMDAR synaptic homeostasis and that GluN2A- and GluN2B-NMDAR synaptic stabilization involves, for part, distinct scaffolding partners, as previously suggested (Lussier et al., 2015). Furthermore, our data demonstrate that a decrease in GluN2A/2B synaptic ratio at CA3-CA1 synapses boosts LTP expression, whereas an increase suppresses it. Indeed, partial depletion of GluN2A-NMDAR at synapses extends the ability to express LTP, whereas decreasing the contribution of GluN2B-NMDAR represses it, as previously suggested (Gardoni et al., 2009). The prominent role of GluN2B-NMDARs in synaptic potentiation could result from their unique ability to interact with and act as a cargo for CaMKII, allowing its fast redistribution and accumulation to dendritic spines, where its activation by calcium influx triggers the induction and maintenance of synaptic potentiation (Bayer et al., 2001; Dupuis et al., 2014; Lisman et al., 2012; Otmakhov et al., 2004). As a consequence, preventing GluN2B-NMDAR synaptic stabilization may interfere with the CaMKII recruitment to dendritic spines and therefore impair LTP expression. Thus, GluN2A- and GluN2B-NMDARs could come as a 2-fold blow, with GluN2A-NMDARs acting as ionotropic calcium providers, while GluN2B-NMDARs provide structural scaffolding support for intracellular partners involved in LTP signaling (Dupuis et al., 2014). Altogether, these pieces of evidence advocate for GluN2A-/GluN2B-NMDAR balance as a kingpin for adaptation at glutamatergic synapses. As the gross number of GluN2A and GluN2B-NMDARs in a hippocampal synapse of the CA1 area is in the range of 20–50 (Shinohara et al., 2008), our data suggest that the lateral redistribution of a limited fraction of NMDARs, as witnessed during LTP (Dupuis et al., 2014), is sufficient to alter the plastic range of a given synapse. Thus, fine tuning of GluN2A and GluN2B-NMDAR nano-organization at synapses emerges as a powerful regulator of neuronal network functions in the hippocampus.

STAR★METHODS

Detailed methods are provided in the online version of this paper and include the following:

- KEY RESOURCES TABLE
- CONTACT FOR REAGENT AND RESOURCE SHARING
- EXPERIMENTAL MODEL AND SUBJECT DETAILS
 - Primary hippocampal cultures
- METHOD DETAILS
 - Transfection
 - Mice cortical neurons and brain lysates preparation
 - Western blot
 - Immunostaining

- Competing ligand synthesis and characterization
- Single Quantum Dot tracking
- Fluorescence microscopy imaging of synaptic proteins
- dSTORM imaging
- Self-interferences (SELI) setup for 3D-SELI-dSTORM
- STED microscopy
- Electrophysiology
- QUANTIFICATION AND STATISTICAL ANALYSIS
 - Co-localization study of synaptic proteins
 - dSTORM data analysis
 - Calculation of localization precision
 - 3D dSTORM image reconstruction analysis
 - STED image analysis
 - Statistics

SUPPLEMENTAL INFORMATION

Supplemental Information includes fourteen figures and two tables and can be found with this article online at <https://doi.org/10.1016/j.neuron.2018.09.012>.

ACKNOWLEDGMENTS

We thank the Bordeaux Imaging Center, a service unit of the CNRS-INSERM and Bordeaux University, and members of the national infrastructure France Biolmaging (ANR-10-INBS-04-01), specially C. Poujol and P. Mascalchi. We also thank Sebastian Malkusch and Mike Heilemann for support in DBSCAN analysis, Christophe Mulle for kindly providing the GluN2A^{+/-} mice, Eric Gouaux for kindly providing antibody directed against the GluN1 subunit, the Plateforme de Biochimie Neurocentre Magendie, Pauline Durand for cell cultures and molecular biology, I. Gauthereau for technical assistance on protein expression, the Proteomic Platform of the Bordeaux Center for Functional Genomics (CGFB) for access to MALDI-TOF, and lab members for constructive discussions. This work was supported by the Erasmus Mundus Joint Doctorate (EMJD) program (European Neuroscience Campus), Programme d'Actions Universitaires Intégrés Luso-Françaises (2016/2017 and 2017/2018), Centre National de la Recherche Scientifique, Agence Nationale de la Recherche (ANR-14-OHRI-0001-01 and ANR-15-CE16-0004-03), IdEx Bordeaux (ANR-10-IDEX-03-02), Fondation pour la Recherche Médicale, Human Frontier Science Program (RGP0019), a postdoctoral Marie-Curie Intra-European fellowship (neuroCHEMbiotools 273817 to D.G.-B.), Conseil Régional d'Aquitaine, a Wellcome Trust Principal Fellowship (101896/Z/13/Z to D.A.R.), ERC advanced grant ADOS (to D.C.), and Labex Bordeaux BRAIN.

AUTHOR CONTRIBUTIONS

B.K. and J.S.F. performed and analyzed super-resolution imaging data. J.D. and L.B. performed and analyzed electrophysiological experiments. D.A.R. provided support for electrophysiological experiments. F.L., J.-B.S., P.B., and L.C. provided expertise and support for image analysis. J.S.F., J.L.-L., P.B., and L.C. performed 3D dSTORM experiments. D.G.-B., D.C., and M.S. generated and validated competing ligands. D.B. generated and validated biological material. B.K., J.S.F., J.D., A.L.C., and L.G. designed the study, planned and analyzed data, and wrote the paper. L.G. supervised the whole project.

DECLARATION OF INTERESTS

The authors declare no competing interests.

Received: September 16, 2017

Revised: April 26, 2018

Accepted: September 5, 2018

Published: September 27, 2018

REFERENCES

- Al-Hallaq, R.A., Conrads, T.P., Veenstra, T.D., and Wenthold, R.J. (2007). NMDA di-heteromeric receptor populations and associated proteins in rat hippocampus. *J. Neurosci.* *27*, 8334–8343.
- Bard, L., and Groc, L. (2011). Glutamate receptor dynamics and protein interaction: lessons from the NMDA receptor. *Mol. Cell. Neurosci.* *48*, 298–307.
- Bard, L., Sainlos, M., Bouchet, D., Cousins, S., Mikasova, L., Breillat, C., Stephenson, F.A., Imperiali, B., Choquet, D., and Groc, L. (2010). Dynamic and specific interaction between synaptic NR2-NMDA receptor and PDZ proteins. *Proc. Natl. Acad. Sci. USA* *107*, 19561–19566.
- Barth, A.L., and Malenka, R.C. (2001). NMDAR EPSC kinetics do not regulate the critical period for LTP at thalamocortical synapses. *Nat. Neurosci.* *4*, 235–236.
- Bartlett, T.E., Bannister, N.J., Collett, V.J., Dargan, S.L., Massey, P.V., Bortolotto, Z.A., Fitzjohn, S.M., Bashir, Z.I., Collingridge, G.L., and Lodge, D. (2007). Differential roles of NR2A and NR2B-containing NMDA receptors in LTP and LTD in the CA1 region of two-week old rat hippocampus. *Neuropharmacology* *52*, 60–70.
- Bayer, K.U., De Koninck, P., Leonard, A.S., Hell, J.W., and Schulman, H. (2001). Interaction with the NMDA receptor locks CaMKII in an active conformation. *Nature* *411*, 801–805.
- Bellone, C., and Nicoll, R.A. (2007). Rapid bidirectional switching of synaptic NMDA receptors. *Neuron* *55*, 779–785.
- Berberich, S., Punnakkal, P., Jensen, V., Pawlak, V., Seeburg, P.H., Hvalby, Ø., and Köhr, G. (2005). Lack of NMDA receptor subtype selectivity for hippocampal long-term potentiation. *J. Neurosci.* *25*, 6907–6910.
- Bon, P., Linarès-Loyez, J., Feyeux, M., Alessandri, K., Lounis, B., Nassoy, P., and Cognet, L. (2018). Self-interference 3D super-resolution microscopy for deep tissue investigations. *Nat. Methods* *15*, 449–454.
- Broadhead, M.J., Horrocks, M.H., Zhu, F., Muresan, L., Benavides-Piccione, R., DeFelipe, J., Fricker, D., Kopanitsa, M.V., Duncan, R.R., Klenerman, D., et al. (2016). PSD95 nanoclusters are postsynaptic building blocks in hippocampus circuits. *Sci. Rep.* *6*, 24626.
- Dudok, B., Barna, L., Ledri, M., Szabó, S.I., Szabadits, E., Pintér, B., Woodhams, S.G., Henstridge, C.M., Balla, G.Y., Nyilas, R., et al. (2015). Cell-specific STORM super-resolution imaging reveals nanoscale organization of cannabinoid signaling. *Nat. Neurosci.* *18*, 75–86.
- Dupuis, J.P., Ladépêche, L., Seth, H., Bard, L., Varela, J., Mikasova, L., Bouchet, D., Rogemond, V., Honnorat, J., Hanse, E., and Groc, L. (2014). Surface dynamics of GluN2B-NMDA receptors controls plasticity of maturing glutamate synapses. *EMBO J.* *33*, 842–861.
- Ehmann, N., van de Linde, S., Alon, A., Ljaschenko, D., Keung, X.Z., Holm, T., Rings, A., DiAntonio, A., Hallermann, S., Ashery, U., et al. (2014). Quantitative super-resolution imaging of Bruchpilot distinguishes active zone states. *Nat. Commun.* *5*, 4650.
- Ferreira, J.S., Schmidt, J., Rio, P., Águas, R., Rooyackers, A., Li, K.W., Smit, A.B., Craig, A.M., and Carvalho, A.L. (2015). GluN2B-Containing NMDA Receptors Regulate AMPA Receptor Traffic through Anchoring of the Synaptic Proteasome. *J. Neurosci.* *35*, 8462–8479.
- Fox, C.J., Russell, K.I., Wang, Y.T., and Christie, B.R. (2006). Contribution of NR2A and NR2B NMDA subunits to bidirectional synaptic plasticity in the hippocampus in vivo. *Hippocampus* *16*, 907–915.
- Frank, R.A., Komiyama, N.H., Ryan, T.J., Zhu, F., O'Dell, T.J., and Grant, S.G. (2016). NMDA receptors are selectively partitioned into complexes and super-complexes during synapse maturation. *Nat. Commun.* *7*, 11264.
- Frost, N.A., Shroff, H., Kong, H., Betzig, E., and Blanpied, T.A. (2010). Single-molecule discrimination of discrete perisynaptic and distributed sites of actin filament assembly within dendritic spines. *Neuron* *67*, 86–99.
- García-Parajo, M.F., Cambi, A., Torreno-Pina, J.A., Thompson, N., and Jacobson, K. (2014). Nanoclustering as a dominant feature of plasma membrane organization. *J. Cell Sci.* *127*, 4995–5005.
- Gardoni, F., Mauceri, D., Malinverno, M., Polli, F., Costa, C., Tozzi, A., Siliquini, S., Picconi, B., Cattabeni, F., Calabresi, P., and Di Luca, M. (2009). Decreased NR2B subunit synaptic levels cause impaired long-term potentiation but not long-term depression. *J. Neurosci.* *29*, 669–677.
- Godin, A.G., Lounis, B., and Cognet, L. (2014). Super-resolution microscopy approaches for live cell imaging. *Biophys. J.* *107*, 1777–1784.
- Gray, J.A., Shi, Y., Usui, H., Doring, M.J., Sakimura, K., and Nicoll, R.A. (2011). Distinct modes of AMPA receptor suppression at developing synapses by GluN2A and GluN2B: single-cell NMDA receptor subunit deletion in vivo. *Neuron* *71*, 1085–1101.
- Heilemann, M., van de Linde, S., Schüttel, M., Kasper, R., Seefeldt, B., Mukherjee, A., Tinnefeld, P., and Sauer, M. (2008). Subdiffraction-resolution fluorescence imaging with conventional fluorescent probes. *Angew. Chem. Int. Ed. Engl.* *47*, 6172–6176.
- Horak, M., Petralia, R.S., Kaniakova, M., and Sans, N. (2014). ER to synapse trafficking of NMDA receptors. *Front. Cell. Neurosci.* *8*, 394.
- Ito, I., Kawakami, R., Sakimura, K., Mishina, M., and Sugiyama, H. (2000). Input-specific targeting of NMDA receptor subtypes at mouse hippocampal CA3 pyramidal neuron synapses. *Neuropharmacology* *39*, 943–951.
- Izumi, Y., Auberson, Y.P., and Zorumski, C.F. (2006). Zinc modulates bidirectional hippocampal plasticity by effects on NMDA receptors. *J. Neurosci.* *26*, 7181–7188.
- Kawakami, R., Shinohara, Y., Kato, Y., Sugiyama, H., Shigemoto, R., and Ito, I. (2003). Asymmetrical allocation of NMDA receptor epsilon2 subunits in hippocampal circuitry. *Science* *300*, 990–994.
- Kutsuwada, T., Sakimura, K., Manabe, T., Takayama, C., Katakura, N., Kushiya, E., Natsume, R., Watanabe, M., Inoue, Y., Yagi, T., et al. (1996). Impairment of suckling response, trigeminal neuronal pattern formation, and hippocampal LTD in NMDA receptor epsilon 2 subunit mutant mice. *Neuron* *16*, 333–344.
- Lau, C.G., and Zukin, R.S. (2007). NMDA receptor trafficking in synaptic plasticity and neuropsychiatric disorders. *Nat. Rev. Neurosci.* *8*, 413–426.
- Lee, C.H., Lü, W., Michel, J.C., Goehring, A., Du, J., Song, X., and Gouaux, E. (2014). NMDA receptor structures reveal subunit arrangement and pore architecture. *Nature* *511*, 191–197.
- Levet, F., Hosy, E., Kechkar, A., Butler, C., Beghin, A., Choquet, D., and Sibarita, J.B. (2015). SR-Tesseler: a method to segment and quantify localization-based super-resolution microscopy data. *Nat. Methods* *12*, 1065–1071.
- Li, R., Huang, F.S., Abbas, A.K., and Wigström, H. (2007). Role of NMDA receptor subtypes in different forms of NMDA-dependent synaptic plasticity. *BMC Neurosci.* *8*, 55.
- Li, P., Banjade, S., Cheng, H.C., Kim, S., Chen, B., Guo, L., Llaguno, M., Hollingsworth, J.V., King, D.S., Banani, S.F., et al. (2012). Phase transitions in the assembly of multivalent signalling proteins. *Nature* *483*, 336–340.
- Lisman, J., Yasuda, R., and Raghavachari, S. (2012). Mechanisms of CaMKII action in long-term potentiation. *Nat. Rev. Neurosci.* *13*, 169–182.
- Liu, L., Wong, T.P., Pozza, M.F., Lingenhoehl, K., Wang, Y., Sheng, M., Auberson, Y.P., and Wang, Y.T. (2004). Role of NMDA receptor subtypes in governing the direction of hippocampal synaptic plasticity. *Science* *304*, 1021–1024.
- Liu, Z., Lavis, L.D., and Betzig, E. (2015). Imaging live-cell dynamics and structure at the single-molecule level. *Mol. Cell* *58*, 644–659.
- Lü, W., Du, J., Goehring, A., and Gouaux, E. (2017). Cryo-EM structures of the trimeric NMDA receptor and its allosteric modulation. *Science* *355*.
- Lussier, M.P., Sanz-Clemente, A., and Roche, K.W. (2015). Dynamic Regulation of N-Methyl-D-aspartate (NMDA) and α -Amino-3-hydroxy-5-methyl-4-isoxazolepropionic Acid (AMPA) Receptors by Posttranslational Modifications. *J. Biol. Chem.* *290*, 28596–28603.
- MacGillavry, H.D., Song, Y., Raghavachari, S., and Blanpied, T.A. (2013). Nanoscale scaffolding domains within the postsynaptic density concentrate synaptic AMPA receptors. *Neuron* *78*, 615–622.

- Malkusch, S., and Heilemann, M. (2016). Extracting quantitative information from single-molecule super-resolution imaging data with LAMA - LocAlization Microscopy Analyzer. *Sci. Rep.* **6**, 34486.
- Matta, J.A., Ashby, M.C., Sanz-Clemente, A., Roche, K.W., and Isaac, J.T. (2011). mGluR5 and NMDA receptors drive the experience- and activity-dependent NMDA receptor NR2B to NR2A subunit switch. *Neuron* **70**, 339–351.
- Monyer, H., Burnashev, N., Laurie, D.J., Sakmann, B., and Seeburg, P.H. (1994). Developmental and regional expression in the rat brain and functional properties of four NMDA receptors. *Neuron* **12**, 529–540.
- Mortensen, K.I., Churchman, L.S., Spudich, J.A., and Flyvbjerg, H. (2010). Optimized localization analysis for single-molecule tracking and super-resolution microscopy. *Nat. Methods* **7**, 377–381.
- Nair, D., Hossy, E., Petersen, J.D., Constals, A., Giannone, G., Choquet, D., and Sibarita, J.B. (2013). Super-resolution imaging reveals that AMPA receptors inside synapses are dynamically organized in nanodomains regulated by PSD95. *J. Neurosci.* **33**, 13204–13224.
- Otmakhov, N., Tao-Cheng, J.H., Carpenter, S., Asrican, B., Dosemeci, A., Reese, T.S., and Lisman, J. (2004). Persistent accumulation of calcium/calmodulin-dependent protein kinase II in dendritic spines after induction of NMDA receptor-dependent chemical long-term potentiation. *J. Neurosci.* **24**, 9324–9331.
- Paoletti, P., Ascher, P., and Neyton, J. (1997). High-affinity zinc inhibition of NMDA NR1-NR2A receptors. *J. Neurosci.* **17**, 5711–5725.
- Paoletti, P., Bellone, C., and Zhou, Q. (2013). NMDA receptor subunit diversity: impact on receptor properties, synaptic plasticity and disease. *Nat. Rev. Neurosci.* **14**, 383–400.
- Park, C.S., Elgersma, Y., Grant, S.G., and Morrison, J.H. (2008). alpha-Isoform of calcium-calmodulin-dependent protein kinase II and postsynaptic density protein 95 differentially regulate synaptic expression of NR2A- and NR2B-containing N-methyl-D-aspartate receptors in hippocampus. *Neuroscience* **151**, 43–55.
- Pennacchietti, F., Vascon, S., Nieuw, T., Rosillo, C., Das, S., Tyagarajan, S.K., Diaspro, A., Del Bue, A., Petrini, E.M., Barberis, A., and Cella Zanacchi, F. (2017). Nanoscale Molecular Reorganization of the Inhibitory Postsynaptic Density Is a Determinant of GABAergic Synaptic Potentiation. *J. Neurosci.* **37**, 1747–1756.
- Rauner, C., and Köhr, G. (2011). Triheteromeric NR1/NR2A/NR2B receptors constitute the major N-methyl-D-aspartate receptor population in adult hippocampal synapses. *J. Biol. Chem.* **286**, 7558–7566.
- Romberg, C., Raffel, J., Martin, L., Sprengel, R., Seeburg, P.H., Rawlins, J.N., Bannerman, D.M., and Paulsen, O. (2009). Induction and expression of GluA1 (GluR-A)-independent LTP in the hippocampus. *Eur. J. Neurosci.* **29**, 1141–1152.
- Sahl, S.J., Hell, S.W., and Jakobs, S. (2017). Fluorescence nanoscopy in cell biology. *Nat. Rev. Mol. Cell Biol.* **18**, 685–701.
- Sainlos, M., Tigaret, C., Poujol, C., Olivier, N.B., Bard, L., Breillat, C., Thiolon, K., Choquet, D., and Imperiali, B. (2011). Biomimetic divalent ligands for the acute disruption of synaptic AMPAR stabilization. *Nat. Chem. Biol.* **7**, 81–91.
- Shinohara, Y., Hirase, H., Watanabe, M., Itakura, M., Takahashi, M., and Shigemoto, R. (2008). Left-right asymmetry of the hippocampal synapses with differential subunit allocation of glutamate receptors. *Proc. Natl. Acad. Sci. USA* **105**, 19498–19503.
- Shipton, O.A., and Paulsen, O. (2013). GluN2A and GluN2B subunit-containing NMDA receptors in hippocampal plasticity. *Philos. Trans. R. Soc. Lond. B Biol. Sci.* **369**, 20130163.
- Smith, G.B., Heynen, A.J., and Bear, M.F. (2009). Bidirectional synaptic mechanisms of ocular dominance plasticity in visual cortex. *Philos. Trans. R. Soc. Lond. B Biol. Sci.* **364**, 357–367.
- Specht, C.G., Izeddin, I., Rodriguez, P.C., El Beheiry, M., Rostaing, P., Darzacq, X., Dahan, M., and Triller, A. (2013). Quantitative nanoscopy of inhibitory synapses: counting gephyrin molecules and receptor binding sites. *Neuron* **79**, 308–321.
- Tang, A.H., Chen, H., Li, T.P., Metzbower, S.R., MacGillavry, H.D., and Blanpied, T.A. (2016). A trans-synaptic nanocolumn aligns neurotransmitter release to receptors. *Nature* **536**, 210–214.
- Thompson, R.E., Larson, D.R., and Webb, W.W. (2002). Precise nanometer localization analysis for individual fluorescent probes. *Biophys. J.* **82**, 2775–2783.
- Vergnano, A.M., Rebola, N., Savtchenko, L.P., Pinheiro, P.S., Casado, M., Kieffer, B.L., Rusakov, D.A., Mülle, C., and Paoletti, P. (2014). Zinc dynamics and action at excitatory synapses. *Neuron* **82**, 1101–1114.
- Volianskis, A., France, G., Jensen, M.S., Bortolotto, Z.A., Jane, D.E., and Collingridge, G.L. (2015). Long-term potentiation and the role of N-methyl-D-aspartate receptors. *Brain Res.* **1621**, 5–16.
- Yashiro, K., and Philpot, B.D. (2008). Regulation of NMDA receptor subunit expression and its implications for LTD, LTP, and metaplasticity. *Neuropharmacology* **55**, 1081–1094.
- Zeng, M., Shang, Y., Araki, Y., Guo, T., Haganir, R.L., and Zhang, M. (2016). Phase Transition in Postsynaptic Densities Underlies Formation of Synaptic Complexes and Synaptic Plasticity. *Cell* **166**, 1163–1175.
- Zhan, H., Stanciuskas, R., Stigloher, C., Dizon, K.K., Jospin, M., Bessereau, J.L., and Pinaud, F. (2014). In vivo single-molecule imaging identifies altered dynamics of calcium channels in dystrophin-mutant *C. elegans*. *Nat. Commun.* **5**, 4974.
- Zhuang, X. (2009). Nano-imaging with Storm. *Nat. Photonics* **3**, 365–367.

STAR★METHODS

KEY RESOURCES TABLE

REAGENT or RESOURCE	SOURCE	IDENTIFIER
Antibodies		
goat anti-guinea pig Alexa 647	Thermo Scientific	Cat#A21450
goat anti-mouse Alexa 488	Thermo Scientific	Cat#A11001
goat anti-mouse Alexa 532	Thermo Scientific	Cat#A11002
goat anti-mouse Alexa 647N	Sigma-Aldrich	Cat#50185
goat anti-rabbit Alexa 647	Thermo Scientific	Cat#A21244
goat anti-rat Alexa 594	Thermo Scientific	Cat#A21471
guinea pig anti-VGLUT	Merck Millipore	Cat#AB5905
mouse anti-flag	Sigma-Aldrich	Cat#F1804
mouse anti-PSD95	Thermo Scientific	Cat#7E3-1B8
mouse anti-GluN1 anti-GluN1	provided by E. Gouaux	clone 10B11
rabbit anti-GluN2A	Agrobio	N/A
rabbit anti-GluN2A	Alomone Labs	Cat#AB_2040025
rabbit anti-GluN2B	Agrobio	N/A
rabbit anti-GluN2B	Alomone Labs	Cat#AB2_040028
rat anti-HA	Roche	Cat#11867423001
mouse anti-beta actin	Sigma-Aldrich	Cat#A5316
Biological Samples		
Embryonic primary hippocampal cultures (details described in Experimental Model and Subject Details below)	This paper	N/A
COS 7 cell line	ECACC	87021302
Chemicals, Peptides, and Recombinant Proteins		
(-)-Bicuculline methochloride	Tocris Bioscience	Cat#0131
D-AP5	Tocris Bioscience	Cat#0106
Ro 25-6981 maleate	Tocris Bioscience	Cat#1594
NBQX disodium salt	Tocris Bioscience	Cat#1044
Tetraspeck microspheres	Thermo Scientific	Cat#T7279
2A-5b	This paper	N/A
2A	This paper	N/A
2B	This paper	N/A
2A ₂	This paper	N/A
2B ₂	This paper	N/A
NS ₂	This paper	N/A
TAT-2A ₂	This paper	N/A
TAT-2B ₂	This paper	N/A
TAT-NS ₂	This paper	N/A
Mowiol 4-88	Millipore	Cat#475904
Experimental Models: Organisms/Strains		
Sprague-Dawley rats	Janvier labs	N/A
GluN2B ^{+/-} C57BL/6 mice	Kutsuwada et al., 1996	N/A
GluN2A ^{+/-} C57BL/6 mice	Sakimura et al., 1995	N/A

(Continued on next page)

Continued

REAGENT or RESOURCE	SOURCE	IDENTIFIER
Recombinant DNA		
GluN1-GFP, C-terminal	Gift from P. de Koninck	N/A
GluN1-SEP, N-terminal	Gift from J. Neyton	N/A
GluN2A-HA, N-terminal	This paper	N/A
GluN2B-flag, N-terminal	This paper	N/A
Software and Algorithms		
Lama software (v 16.10)	(Malkusch and Heilemann, 2016)	http://user.uni-frankfurt.de/~malkusch/lama.html
Prism 5.03 software	GraphPad	https://www.graphpad.com/scientific-software/prism/
MetaMorph Offline software (7.8.9.0)	Molecular Devices	https://www.moleculardevices.com/products/cellular-imaging-systems/acquisition-and-analysis-software/metamorph-microscopy
ImageJ software (1.50b)	National Institutes of Health	https://imagej.nih.gov/ij
SR-Tesseler software	Levet et al., 2015	http://www.iins.u-bordeaux.fr/team-sibarita-SR-Tesseler
Leica LAS software	Leica Microsystems	https://www.leica-microsystems.com/products/microscope-software/details/product/leica-las-x-ls/
Density-based spatial clustering of applications with noise (DBSCAN) algorithm	(Malkusch and Heilemann, 2016) Lama software	http://user.uni-frankfurt.de/~malkusch/lama.html
pClamp 10 software	Molecular Devices	https://www.moleculardevices.com/products/axon-patch-clamp-system/acquisition-and-analysis-software/pclamp-software-suite

CONTACT FOR REAGENT AND RESOURCE SHARING

Further information and requests for resources and reagents should be directed to and will be fulfilled by the Lead Contact, Laurent Groc (laurent.groc@u-bordeaux.fr).

EXPERIMENTAL MODEL AND SUBJECT DETAILS

All the procedures were conducted in accordance with the guidelines of the University of Bordeaux / CNRS Animal Care and Use Committee.

Primary hippocampal cultures

Primary hippocampal cultures were prepared from 18 day embryonic Sprague-Dawley rats. Briefly, hippocampi were dissected and collected in HBSS containing Penicillin-Streptomycin (PS) and HEPES. Tissues were dissociated with Trypsin-EDTA/PS/HEPES and neurons were plated in minimum essential medium supplemented with 10% horse serum on coverslips coated with 1 mg/mL poly-L-lysine (PLL) in 60 mm Petri dishes at a density of either 150,000, for immunostaining, or 250,000 cells, for transfection, per dish. Following neuronal attachment to the surface, the coverslips were flipped on top of a glial cell monolayer in Neurobasal medium supplemented with L-glutamine (GIBCO, #25030-024) and NeuroCult SM1 Neuronal Supplement (StemCell Technologies, #05711). Cells were maintained at 36.5°C with 5% CO₂.

METHOD DETAILS

Transfection

Neurons were transfected at DIV 9-11 using the calcium-phosphate coprecipitation method. Precipitates containing 1-1.5 µg plasmidic DNA (GluN1-SEP for fluorescence microscopy or GluN1-GFP/GluN2A-HA/GluN2B-flag for STED) were prepared using the following solutions: TE (1mM Tris-HCl pH 7.3, 1mM EDTA), CaCl₂ (2.5 M CaCl₂ in 10 mM HEPES, pH 7.2), 2 × HEPES-buffered saline (HEBS; 12 mM dextrose, 50 mM HEPES, 10 mM KCl, 280 mM NaCl and 1.5 mM Na₂HPO₄·2H₂O, pH 7.2). Coverslips containing neurons were moved to 12 well multiwell plates containing 200 µl/well of conditioned culture medium. The 50 µl precipitate solution was added to each well, in the presence of 2 mM kynurenic acid (Sigma-Aldrich #K3375) and incubated for 1 h at 37°C. Afterward,

cells were washed with unsupplemented Neurobasal medium containing 2 mM kynurenic acid and moved back to their original culture dish for 4 days of expression before use.

COS-7 were cultured in DMEM (Biowest, #L0102) with 10% FBS (GIBCO), 2 mM glutamine (PAA). Transient transfections with GluN2A-SEP/GluN1 or GluN2B/GluN1 plasmids were performed 2 days before lysis, using Amaxa Nucleofector (Lonza).

Mice cortical neurons and brain lysates preparation

GluN2B^{+/+} and GluN2B^{-/-} cortical cultures and cells lysates were prepared as previously described (Ferreira et al., 2015). GluN2A^{+/+} and GluN2A^{-/-} brains from P15 mice (Vergnano et al., 2014) were dissected and frozen in liquid nitrogen. Brains were thawed in 1.5 mL of ice-cold sucrose buffer (0.32 M sucrose, 1 mM HEPES, 1 mM MgCl₂, 1 mM NaHCO₃ and a protease inhibitor cocktail –1:1000, Calbiochem) and homogenized with a Teflon glass potter. After centrifugation (1,000 g, 10 min at 4°C), the supernatant was centrifuged once again at 13 000 g for 30 min at 4°C. The resulting pellet (membranes enriched fraction) was resuspended with 0.5 mL of solubilization buffer (20 mM Tris pH8.0, 1 mM EDTA, 1.3% triton and protease inhibitor cocktail) and quantified before use.

Western blot

Cortical neuronal cultures were prepared with 5x SDS-PAGE Sample Loading Buffer (Nzytech genes & enzymes, #MB11701) to a concentration of 1 µg/µl and brains samples were prepared with 2x sample buffer to load 5 µg of total protein per well. Samples were boiled 5 min at 95°C and separated by SDS/PAGE (4%–15% Mini-PROTEAN TGX Gel-Biorad) for 40 min at 200V. Gels were then blotted onto nitrocellulose membrane during 1 h at 100V. After blocking 1h in 5% milk in Tris-saline - 0.05% tween 20 (TBST), the membranes were hybridized with the primary antibodies: custom-made anti-GluN2A (rabbit polyclonal, 2 µg/mL, Agrobio), custom-made anti-GluN2B (rabbit polyclonal, 2 µg/mL, Agrobio) or anti-Actin as loading control (mouse monoclonal, 1/5000) diluted in TBST 0.5% milk, during 1h30 at room temperature. Corresponding secondary HRP antibodies were used at 1:5000 in TBST 0.5% milk. Detection was performed using the SuperSignal West Femto Maximum Sensitivity Substrate detection kit (ThermoFisher Scientific, Pierce, #34095) revealed with the Chemidoc system (Biorad).

Immunostaining

The following primary antibodies were used: anti-flag (Sigma-Aldrich #F1804, 2 µg/mL), anti-GluN1 (clone 10B11, provided by E. Gouaux), anti-GluN2A (Agrobio, custom-made, epitope: GHSHDVTERELRN(C), 0.1 mg/mL), anti-GluN2B (Agrobio, custom-made, epitope: (C)NTHEKRIYQSNMLNR, 0.1 mg/mL), anti-HA (Roche #11867423001, 0.5 µg/mL), anti-PSD95 (Thermo Scientific #7E3-1B8, 1 µg/mL), anti-VGLUT (Merck #AB5905), anti-GFP (Thermo Scientific #A6455). All secondary antibodies were used at 0.1mg/mL concentration: anti-guinea pig Alexa 647 (Thermo Scientific #A21450), anti-mouse Alexa 488 (Thermo Scientific #A11001), anti-mouse Alexa 532 (Thermo Scientific #A11002), anti-mouse Atto 647N (Sigma-Aldrich #50185), anti-rabbit Alexa 568 (Thermo Scientific #A11011), anti-rabbit Alexa 647 (Thermo Scientific #A21244), anti-rabbit Alexa 488 (Thermo Scientific #A11008), anti-rat Alexa 594 (Thermo Scientific #A21471).

Live neurons were surface immunostained for endogenous or overexpressed (GluN2A-HA, GluN2B-flag, GluN1-SEP) GluN2A and/or GluN2B for 15 min at 37°C using specific antibodies. After fixation (4% paraformaldehyde (Sigma-Aldrich, #P6148)/4% sucrose (Sigma-Aldrich, #0389) in PBS, 15 min) at room temperature (RT), neurons were permeabilized with 0.4% Triton X-100 (5 min) and treated with a blocking solution containing 1.5% bovine serum albumin (BSA, Sigma-Aldrich, #A3059)/0.1% fish skin gelatin/0.1% Triton X-100 for 40 min. Cells were then successively incubated with the second primary antibodies, when indicated, for 45 min at RT. The secondary antibodies were used during 30 min incubation at RT and, after an additional wash, the cells were mounted in Mowiol mounting medium. For dSTORM imaging, a second fixation was performed after incubation with the secondary antibodies and cells were kept in PBS at 4°C until imaging. COS7 cells were fixed in 4% paraformaldehyde/4% sucrose in PBS, incubated 10 min with PBS plus 50 mM NH₄Cl (Sigma-Aldrich, #A4514), permeabilized with 0.25% Triton X-100 (Sigma-Aldrich, #9002-93) in PBS (5 min) and incubated with 10% BSA in PBS for 1h at RT, to block non-specific labeling. Antibodies were prepared in 3% BSA in PBS. Primary antibodies were incubated for 2h and secondary antibodies 1h at RT. Between each incubation cells were washed with PBS (Euromedex, #ET330).

Competing ligand synthesis and characterization

Chemicals and abbreviations

Fmoc-protected amino acids were from GenScript USA (Piscataway, NJ USA) and Fmoc-Val-Nova syn TGA resin and Fmoc-PAL-NOVA PEG resins (Darmstadt, Germany). HBTU was from Iris Biotech GmbH (Marktredwitz, Germany). Sodium phosphate monobasic, Sodium phosphate dibasic, CuI, CuSO₄, ascorbic acid, sodium ascorbate, Aminoguanidine · HCl, THPTA, HOBt, DIPEA, 4-methylpiperidine, acetic anhydride, Phenylsilane, Pd(PPh₃)₄, pyridine, TIPS and DHB were from Sigma-Aldrich (Steinheim, Germany). TFA, MeCN, DCM, DMF and diethyl ether were from Fisher Scientific (Loughborough, UK). Fmoc-Dab(Alloc)-OH was from Bachem AG (Budendorf, Switzerland) and NMP was from Applied Biosystems (Warrington, UK). Abbreviations: 4-DMAP, 4-dimethylaminophthalimide; DCM, dichloromethane; DHB, 2,5-Dihydroxybenzoic acid; DIPEA, N-N'-diisopropylethylamine; DMF, N,N-dimethylformamide; HOBt, 1-hydroxybenzotriazole; RP-HPLC, reverse phase high performance liquid chromatography; MALDI, matrix-assisted laser desorption ionisation; MeCN, acetonitrile; MS, mass spectrometry; NMP, N-methyl-2-pyrrolidone; SPPS, solid

phase peptide synthesis; HBTU, 2-(1H-Benzotriazol-1-yl)-1,1,3,3-tetramethyluronium hexafluorophosphate; TFA, trifluoroacetic acid; THPTA, tris(3-hydroxypropyltriethylmethyl)amine; TIPS, triisopropylsilane; Amino acid symbols denote the L configuration unless otherwise stated. All reported solvent ratios are expressed as volume/volume unless indicated otherwise.

General peptide synthesis

Peptides were synthesized at 0.05 mmol scale. Amino acids were assembled by automated solid phase peptide synthesis on a CEM μ waves Liberty-1 synthesizer (Saclay, France) following standard coupling protocols. Briefly, Fmoc groups were cleaved with 4-methylpiperidine in DMF (1:5) containing 0.1M HOBt using a combination of short (35 W, 75°C, 30 s) and a long cycle (35 W, 70°C, 180 s). Couplings of Fmoc-protected amino acid (0.2 M) were carried out in the presence of HBTU (0.25 M) and DIPEA (1M) using standard coupling cycles (20 W, 70°C, 300 s) except for *Fmoc-Arg(Pbf)-OH* (0 W, RT, 1500 s followed by 20 W, 70°C, 300 s). Methionine was systematically replaced by Norleucine, a more stable isostere. For the fluorescent probe, serine at position –5 from the original 2A₁₅ sequence was substituted by diamino butyric acid protected with the alloc group on the lateral chain. For the TAT sequence, a Tyr is introduced at the N terminus for quantification purposes. The free N terminus of the TAT peptide was manually functionalized by an azide (Fmoc-Lys(N₃)-OH) and acetylated.

Dimerization and functionalization

Divalent ligands were obtained by using copper-catalyzed click chemistry on resin harboring a mix of a sequences functionalized by azide (Fmoc-Lys(N₃)-OH) and alkyne (Pentynoic acid) groups as described previously (Sainlos et al., 2011). We used a slight modification to the previously described protocol (Sainlos et al., 2011). In our case we used a 3.5:7 mixture of alkyne (Pentynoic acid) and azide (Fmoc-Lys(N₃)-OH) instead of the 3:7 mixture used previously (Sainlos et al., 2011). The ligands were either acetyl capped or further processed to incorporate a TAT sequence. N-terminal amino groups were capped with acetyl group. Acetylation was performed using a solution of acetic anhydride (0.15 M) and pyridine (0.15 M) in DMF for 1h30 min. After cleavage and purification of the ligands and the TAT sequence using a standard protocol (see below), the two fragments were coupled using copper-catalyzed click chemistry in solution to purified divalent ligands containing an alkyne (Pentynoic acid) group at the N terminus. Briefly, The Ac-Lys(N₃)-TAT-OH (600 nmol) and the N terminus alkyne derived divalent ligand (300 nmol) were dissolved in 300 μ L each of 200 mM pH 8 phosphate buffer degassed with argon. The TAT solution was added to the alkyne solution dropwise, then 2.6 μ L of aminoguanidine·HCl in H₂O (1 M) were added to the mixture of the ligands and mixed carefully. A mixture of 4.9 μ L of 250 mM CuSO₄ in H₂O with 40.8 μ L of THPTA (50mM) was prepared, mixed after which 20 μ L were added to the mixture containing the ligands and mixed carefully. Finally, 2.5 μ L of sodium ascorbate in H₂O (500mM) were added to the mixture of ligands, mixed and reacted overnight at 25°C and 1400 rpm. The solutions were kept under argon the whole procedure. The reaction was quenched by adding 1 mL of H₂O with 0.1% TFA and the mixture was directly purified by semi-preparative HPLC following the standard protocols (see below).

Peptide-base ligands cleavage and purification

Ligands were cleaved from the resin for 3 h using TFA/H₂O/TIPS (95:2.5:2.5) with mild orbital shaking and precipitated with cold diethyl ether. Crude peptides were resuspended in 1 mL of DMF followed by 9 mL of H₂O and purified by RP-HPLC with a semi-preparative column (YMC C18, ODS-A 5/120, 250 \times 20 mm) on a Waters 1525 HPLC system equipped with a UV/Vis detector and using a standard gradient (5% MeCN containing 0.1% TFA for 5 min followed by an appropriate gradient for 40 min of MeCN containing 0.1% TFA in H₂O containing 0.1% TFA at a flow rate of 1 mL·min⁻¹ and UV detection at 228 and 350 nm). The ligands were characterized by analytical RP-HPLC and MALDI-TOF. All the ligands were more than 90% pure as judged by analytical RP-HPLC. The ligands were lyophilized and stored at –80°C until usage.

Affinity determination

The first two PDZ domains of PSD-95 (PSD-95-12) was expressed and purified as previously described (Sainlos et al., 2011). Briefly, the first two PDZ domain of PSD-95 were expressed using a home-made vector derived from pET-32 that present an octa-histidine tag just after the initial methionine followed by a TEV cleavage just before the gene. Expression was performed in BL21 codon plus (DE3)-RIPL by auto-induction at 16°C for 16 hr. The harvested cells were lysed and the protein purified in non-denaturing conditions by Ni-NTA affinity chromatography. The polyHis tag was removed by treatment with home-produced TEV protease and the protein was further purified to homogeneity by size exclusion chromatography (Superdex 75 Hiload 16/60 column) in PBS. The protein was finally concentrated to about 2-3 mg/mL and stored at –80°C until used. All titration experiments were carried out at 25°C in PBS (10 mM Phosphate, 150 mM NaCl, pH 7.4) in a fluorimeter (Fluoromax-4, HORIBA Jobin Yvon). Fluorescence was measured in arbitrary units. Samples were excited at 421 nm (4-DMAP excitation). Slit widths were 3 nm for excitation and 6 nm for emission. The emission spectra were recorded in triplicate without averaging between 470 and 750 nm (0.5 nm and 0.1 s integration time). For the direct titration of 2A₁₅ monovalent ligand labeled with an environment sensitive fluorophore, 4-DMAP labeled 2A₁₅ monovalent ligand (0.96 μ M) was titrated against a broad range of increasing amounts PSD-95-12 in a 130 μ L final volume using a 1 cm path length quartz cuvette. Titration curves were fitted and analyzed with GraphPad Prism v5.3 for Windows. For the competitive titration of non-fluorescent ligands, 4-DMAP labeled ligand (8.1 μ M) was equilibrated with PSD-95-12 protein (4.0 μ M) in a 1 cm path length quartz cuvette in 450 μ L (total volume). Non-labeled competitor was titrated in the cuvette using high concentration stock solutions. The loss of fluorescence of the peptide labeled with the environment sensitive fluorophore (4-DMAP) was monitored to assess the competition process with the non-labeled ligand. For each competitive titration curve, fluorescence levels were normalized by using the initial fluorescence values obtained in the presence of the fluorescent probe and PDZ domain recombinant protein and final value to be 0 as consequence of loss of fluorescence in the presence of the competitor at 540 nm.

Single Quantum Dot tracking

Cultured hippocampal neurons at DIV 10–14 were incubated 10 min with 1 μ l of polyclonal antibodies against GluN2B or GluN2A subunits (Alomone Labs, Jerusalem, Israel; epitope correspond to residues 323–337 of GluN2B subunit, #AB_2040028, or residues 41–53 of GluN2A subunit, # AB_2040025, 1:200) followed by 10 min incubation with Quantum Dots (QD) 655 Goat F(ab')₂ anti-rabbit polyclonal antibodies (Invitrogen, Thermo Fisher Scientific Inc., Cambridge, United Kingdom, 1:10000). Cells were then incubated for 30 s with 20 nM MitoTracker Green FM (Thermo Scientific #M7514). All incubations were done in Neurobasal Medium supplemented with 1% BSA at 37°C. Coverslips were mounted in tyrode solution (30 mM D-glucose, 120 mM NaCl, 5 mM KCl, 2 mM MgCl₂, 2 mM CaCl₂ and 25 mM HEPES, pH 7.3–7.4) on a heated-chamber for observation. QD were detected by using a mercury lamp and appropriate excitation/emission filters. Images were obtained with an acquisition time of 50 ms (20 Hz) with up to 500 consecutive frames. Signals were detected using an EMCCD camera (Evolve, Photometrics). TAT-2A₂, TAT-2B₂ or TAT-NS₂ ligands (10 μ M) were incubated 20 min before QD labeling and acquisition. QD recording sessions, which lasted up to 20–25 min, were processed with the Metamorph software. The instantaneous diffusion coefficient 'D' was calculated for each trajectory, from linear fits of the first 4 points of the mean-square-displacement versus time function using $MSD(t) = \langle r^2 \rangle (t) = 4Dt$. The two-dimensional trajectories of single molecules in the plane of focus were constructed by correlation analysis between consecutive images using a Vogel algorithm. This technique provides with a high accuracy of single QD detection (~30 nm resolution) which we used to measure the dynamic distribution of GluN2B-NMDAR or GluN2A-NMDAR at synaptic sites. Synaptic area was defined with MitoTracker. The synaptic diffusion coefficient was calculated from GluN2-QD trajectories that were only present inside the synaptic area.

Fluorescence microscopy imaging of synaptic proteins

Neuronal fluorescence images were acquired using an Electron Multiplying Charged Coupled Device (EMCCD) Photometrics Quantem 512 camera and MetaMorph imaging software (Molecular Devices), on an inverted confocal spinning-disk microscope (Leica DMI6000B, Leica), with a Leica HCX PL APO CS 63x/1.4 oil objective. For each experiment, images in each channel (SPI lasers 488/568/647, quad simple filters) were captured using the same laser intensity and exposure time across all fixed cells; images were acquired as gray scale from individual channels and pseudocolor overlays were prepared using ImageJ. COS7 cells fluorescence images were acquired using a Cool Snap HQ2 CCD camera (Photometrics) and NIS – Elements Imaging Software (version 4.12, Nikon), on an inverted Nikon Eclipse Ti-S microscope, with a Nikon Plan Apo VC 60x/1.4 oil objective. Images were prepared using ImageJ.

dSTORM imaging

All imaging sessions were performed using a commercial Leica SR GSD microscope (Leica Microsystems, Wetzlar, Germany) equipped with a Leica HC PL APO 160x/1.43 NA oil immersion TIRF objective enabling detection of single fluorophores and an EMCCD iXon camera (ANDOR, Belfast, UK). Samples were illuminated in TIRF mode and images were obtained with an exposure time of 10.85 ms with up to 100,000 consecutive frames. Imaging was carried out at room temperature in a closed Ludin chamber (Life Imaging Services, Switzerland) using a pH-adjusted extracellular solution containing oxygen scavengers and reducing agents (Heilemann et al., 2008). When the field of interest was chosen a snapshot was taken of the epifluorescence labeling of NMDAR and PSD95. Image acquisition was controlled by the Leica LAS software. First, the ensemble fluorescence of Alexa 647 was converted into dark state using 50% of full power of the 642 nm laser (500 mW). Once the desired number of single fluorophores per frame was reached, the intensity of the 642 nm laser was reduced to 15% of full laser power and kept at this level during acquisition. In order to keep an optimal number of stochastically activated molecules per frame the intensity of the 405 nm laser (30 mW) was continuously adjusted reaching a maximum of 10% of full laser power. The particle detection threshold was set to 15 in the Leica LAS software. For two-color dSTORM imaging, the 642 nm and 532 nm (1000 mW) lasers was used sequentially with similar settings as above. Super-resolution images were reconstructed by the Leica LAS software using a fitting algorithm determining the centroid-coordinates of a single molecule and fitting the point-spread-function (PSF) of a distinct diffraction limited event to a Gaussian function. The generated super-resolved images had a final spatial resolution of 40 nm. Multicolor fluorescent microspheres (#T7279 TetraSpeck, Life Technologies) were used for lateral drift correction.

Self-interferences (SELI) setup for 3D-SELI-dSTORM

SELI-dSTORM was performed on a commercial inverted microscope (TiE, Nikon) equipped with a 60x NA = 1.45 oil objective (Nikon) and a double-stage filter set to allow simultaneous imaging of fluorescence imaging of Alexa Fluor 647 fluorophores and transmission light at $\lambda = 561 \pm 10$ nm for 3D drift correction. Fluorophores are excited by a 638 nm laser diode (HL63193, Oclaro) in wide-field epi-configuration while the transmission white light is emitted by a halogen lamp (Nikon) filtered at 561 ± 10 nm (Semrock), distinct from the excitation and the emission fluorescence bands. Blinking of the Alexa Fluor 647 dyes was reactivated by 405 nm illumination (Intensilight, Nikon, Japan and + 395/20 nm Semrock filter). The SELI fluorescence detection path is composed of a phase-only diffraction grating inserted close to the imaging plane of the microscope output port and optically relayed by a dual-doublet telescope on a sCMOS sensor (Orca Flash 4, Hamamatsu). The diffraction grating generates self-interferences within the microscope point-spread function to simultaneously encode equiphase and intensity fluorescence signals carrying the 3D position of an emitter. Images are recorded with an integration time of 30 ms per frame during 20 min in average. All data were processed using custom made programs coded in the Labview environment (National Instrument).

STED microscopy

All STED imaging sessions were carried out on a Leica DMI6000 TCS SP8 X system equipped with two continuous wave STED lasers for excitation at 592 nm and 660 nm and a pulsed 775 nm depletion laser. A 40X/1.3 NA oil immersion objective was used to identify transfected cells, while a 100X/1.4 NA oil immersion objective lens was used for STED imaging. Fluorescence signals were passed through a pinhole size of 1 Airy unit. Image frame size was adjusted per image and acquired sequentially in line-scan mode using a scan speed of 400 Hz with a pixel size of 20 nm.

Electrophysiology

P15-P21 C57BL/6 mice were anesthetized using isoflurane. Parasagittal brain slices (350 μm thick) were prepared in a dissection solution containing (in mM): 250 sucrose, 2 KCl, 7 MgCl_2 , 0.5 CaCl_2 , 1.15 NaH_2PO_4 , 11 glucose and 26 NaHCO_3 (equilibrated with 95% O_2 /5% CO_2). Slices were then incubated at 33°C for 30 min and subsequently stored at room temperature in an oxygenated artificial cerebrospinal fluid (aCSF; gassed with 95% O_2 and 5% CO_2) containing (in mM): 126 NaCl, 3.5 KCl, 2 CaCl_2 , 1.3 MgCl_2 , 1.2 NaH_2PO_4 , 25 NaHCO_3 and 12.1 glucose (pH 7.35). Whole-cell voltage-clamp recordings from CA1 pyramidal were made at 33°C cells under infrared differential interference contrast imaging. EPSCs were evoked at a rate of 0.05 Hz via an aCSF-filled glass micro-electrode positioned in the *stratum radiatum* to stimulate Schaffer collaterals. Evoked NMDA-mediated excitatory postsynaptic currents (eEPSCs) were recorded at +40 mV in the presence of the GABAA receptor antagonist bicuculline (20 μM) and the AMPA receptor antagonist NBQX (10 μM). Ro 25-6981 (2 μM) and Zn^{2+} (250 nM) were added when required to selectively inhibit GluN2B- or GluN2A-NMDAR, respectively. Zn^{2+} (250 nM) was prepared from ZnCl_2 dissolved in Tricine 10 mM with the relation $[\text{Zinc}]_{\text{free}} = [\text{Zinc}]_{\text{applied}}/200$. At this concentration, Zn^{2+} acts as a partial antagonist that selectively inhibits ~70%–80% of the current flowing through GluN2A-containing NMDAR (GluN1/GluN1/GluN2A/GluN2A) (Paoletti et al., 1997). All drugs were obtained from Tocris Bioscience (Bristol, UK) or Sigma-Aldrich (St. Louis, MO). Recording electrodes (4–5 $\text{M}\Omega$) were filled with a solution containing (in mM): 125 cesium methanesulfonate, 4 NaCl, 2 MgCl_2 , 10 HEPES, 10 EGTA, 5 phosphocreatine, 2 MgATP, 0.33 mM Na_3GTP and 5 μM of either the 2A_2 , 2B_2 or the NS_2 ligands (adjusted to pH 7.2 with CsOH). For LTP experiments, the intracellular solution contained 125 mM cesium gluconate, 8 mM NaCl, 10 mM HEPES, 0.2 mM EGTA, 4 mM Mg-ATP, 0.33 Na_3GTP , 10 mM phosphocreatine, 5 mM TEA-Cl and 5 μM of either the 2A_2 , 2B_2 or the NS_2 ligands (adjusted to pH 7.3 with CsOH). EPSCs were recorded at –60 mV in presence of bicuculline (20 μM). LTP was induced by a pairing protocol consisting of 200 Schaffer collateral stimulations at 2 Hz while depolarizing the postsynaptic cell to –5 mV. Data were recorded using a Multiclamp 700B amplifier and a Digidata 1550B interface controlled by Clampex 10.7 (Molecular Devices). Series resistance was monitored throughout the experiment by a brief voltage step of 5 mV at the beginning of each recording, and data were discarded when it changed by > 20%.

QUANTIFICATION AND STATISTICAL ANALYSIS

Co-localization study of synaptic proteins

To quantify the immunocytochemistry data, 19–22 cells were selected. From each neuron, two to three dendrites were chosen for analysis. The images were subjected to a user-defined intensity threshold, for cluster selection and background subtraction. Number of clusters was measured for all selected regions and normalized to the dendrite length. Synaptic clusters were determined as the postsynaptic clusters overlapping the thresholded image of PSD95 (postsynaptic) or VGLUT (presynaptic).

dSTORM data analysis

Three complementary analysis methods relying on different principles were used to characterize the nanoscopic organization of NMDAR. While the wavelet-based morphometric analysis uses reconstructed super-resolved images and performs a segmentation to distinguish signals from background, both DBSCAN and SR-Tesseler analyses utilize localization coordinates. In DBSCAN, the cluster area is measured based on localization density within a given radius (related to the size of the protein of interest with its labeling, without considering the background), while the SR-Tesseler distinguishes clusters or nanodomains based on local increases in localization density compared to average background or average cluster density, respectively (the size of the protein and labeling are not taken into account).

Wavelet-based morphometric image analysis (image-based analysis)

Super-resolution images were reconstructed by the Leica LAS software using a fitting algorithm determining the centroid-coordinates of a single molecule and fitting the point-spread-function (PSF) of a distinct diffraction limited event to a Gaussian function. NMDAR or PSD95 clusters were identified on their respective epifluorescence images. GluN2A- or GluN2B-NMDAR nanodomain number, area and shape were quantified after segmentation of their respective dSTORM reconstructed images (MetaMorph software, Molecular Devices). Morphological features, such as surface area, length and shape of each segmented structure, were exported to calculate their respective distributions. The dimensions were computed by 2D anisotropic Gaussian fitting, from which the principal and the auxiliary axes were extracted as 2.3σ long and 2.3σ short, respectively. The shape factor was calculated as a ratio between the auxiliary and the principal axes. The epifluorescence image of PSD95 was superimposed on the NMDAR dSTORM image to identify the PSD95 positive (PSD95+) versus PSD95 negative (PSD95-) nanodomains.

Density-based analysis

The previously described density-based spatial clustering of applications with noise (DBSCAN) algorithm, implemented in the Lama software (Malkusch and Heilemann, 2016), was used to calculate the area and molecule number of NMDAR clusters. The DBSCAN algorithm identifies the localizations that reside within the middle of a circle of the observation radius (ϵ) and enclose at least P_{\min} (minimal cluster size) localizations. An ϵ of 14 nm was chosen which roughly corresponds to the radius of an NMDAR (Lee et al., 2014) with the antibody complex attached to it. The P_{\min} was chosen based on the density-distribution of the localizations within ϵ ; in our case the value was 6 in order to separate the localizations from noise but not too large to find sparse clusters. The cluster localizations were corrected for fluorophore blinking, a function included in the Lama software (Malkusch and Heilemann, 2016), and normalized to the corresponding image background to estimate the number of molecules per clusters from the number of localizations.

SR-Tesseler analysis

The previously described SR-Tesseler method was used (Levet et al., 2015) to analyze both clusters and nanodomains. Single molecule localization coordinates were used to compute a Voronoi tessellation, in order to partition the image space in polygons of various sizes centered on each localized molecule. First-rank densities δ_i^1 were computed and density maps were generated by texturing the Voronoi polygons with δ_i^1 values. Segmentations of the clusters were performed by applying a threshold of twice the average density $\bar{\delta}$ of the whole dataset, with a minimum area of 2 and a minimum number of localizations of 5. Clusters' nanodomains were identified by applying a threshold of one time the average density of each cluster (0.01 minimum area, 25 minimum number of localizations). All selected neighboring molecules were merged together to segment clusters and nanodomains, and the size parameters were extracted by principal component analysis.

SR-Tesseler colocalization analysis

We used multicolor fluorescent microbeads as fiducial markers to correct for lateral drifts and register multicolor experimental data. Each color was segmented independently using the two-level tessellation-based segmentation described above. Colocalization was computed as the overlapping surface between the channels.

Calculation of localization precision

Theoretical localization precision was calculated from the integrated intensity of single PSFs using the methods of Thompson and Mortensen (Mortensen et al., 2010; Thompson et al., 2002) implemented in the Lama software (Malkusch and Heilemann, 2016). Both of these methods utilize PSFs calculated based on 'least-squares estimation' (LSE). Localization precision depends mainly on the number of detected photons (N) and the standard deviation of the PSF (σ), both of which depend on characteristics of the optical setup and the type of fluorescent labeling used. Additionally, localization precision depends also on the area imaged in one pixel of the camera chip (a) and the background signal (b). Our Leica SR GSD 3D system, with AlexaFluor 647 labeling, had a σ value of 140 nm (σ), and a noise value of 8.4 (b).

3D dSTORM image reconstruction analysis

Each single molecule position was obtained by a 2D elliptic Gaussian fitting of the PSF. The lateral position is given by the PSF centroid while the axial position is obtained by comparing the fitted parameters to a calibration curve (Huang et al., 2008). Super-resolution image reconstruction and cluster visualization for counting were performed using homemade LABVIEW software. Nanodomains were user-defined in the 3D-reconstructed dSTORM image as individualized groups of localizations, spatially separated in the 3 dimensions. Single isolated localizations were not taken into account.

STED image analysis

For analysis, five NMDAR clusters expressing both GluN2A-HA and GluN2B-flag were selected per single STED image for a total of 22 images from two separate experiments. The selected clusters were subjected to a user-defined intensity threshold and cluster area was measured afterward. GluN2A fraction over GluN2B was calculated as the overlapping GluN2A area on GluN2B area, normalized to the total GluN2A area.

Statistics

The statistical analysis was performed with the help of GraphPad Prism 5 software (GraphPad Software). The different statistical tests used are indicated in Table S1.